

A Dissertation Submitted for a Doctorate in Materials Science

Plasmonic Nanoengineering in Hollow Metal Nanostructures: An Electron Energy-Loss Spectroscopy Study

Aziz Genç

Supervisor: Prof. Jordi Arbiol i Cobos

Tutor: Dr. Xavier Granados i García

Universitat Autònoma de Barcelona
Department of Physics, Faculty of Sciences

Institut de Ciència de Materials de Barcelona (ICMAB-CSIC)
Institut Català de Nanociència i Nanotecnologia (ICN2)



July 2015

Chapter 3

Plasmonic Nanoengineering in Complex Metal Nanostructures: From Solid Nanocubes to Hollow Multi-walled Nanoboxes

3.1 Introduction

In this chapter, we present a comprehensive EELS study on the evolution of LSPRs in complex metal nanostructures. By engineering nanostructures from solid Ag nanocubes to hollow AuAg multi-walled nanoboxes, we have been able to reveal the properties (spatial distributions of plasmon energy and/or intensities) of different LSPRs arising due to different structural features. We experimentally investigate the in-plane 2D distribution of the LSPRs of Ag nanocubes and various AuAg hollow monocrystalline nanostructures [69] ~ 50 nm in size with sub-eV and nanometer resolutions. LSPR nanoscale maps have been systematically obtained on: i) Ag cube, ii) Ag@Au core-shell nanocube, iii) pinholed and iv) single-walled AuAg nanoboxes, v) AuAg nanoframe and vi) double-walled AuAg nanobox, by means of EELS spectrum imaging (SI) [206], allowing to unravel the full modal spectrum, bright and dark modes, of the plasmonic nanocavities [224]. We demonstrate, by direct measurements, the presence of different LSPR modes arising due to the hollow nature of the samples and correlate our findings with boundary element method (BEM) [282]. The distribution of the plasmon resonances are explained based on the plasmon hybridization mechanism [63].

As mentioned in the previous chapter, surface plasmon resonances are collective oscillations of conduction electron in a material excited by an electromagnetic wave [290]. Such a unique optical property have enabled usage of plasmonic nanostructures as building blocks for nano optics and various novel applications including, but not limited to, sensor devices [126], surface enhanced Raman spectroscopy (SERS) [127], theranostics [68], photovoltaics [128], thanks to their ability of localization of light at nanoscale, far beyond the diffraction limit of electromagnetic waves in dielectric media [1, 291]. This chapter has two main aims: (i) detailed characterization and understanding of the nanoscale plasmonic properties of complex AuAg nanostructures at different stages of galvanic replacement reaction and (ii) explore the possibility of using these complex hollow nanostructures as efficient sensors for biosensing experiments and correlate their sensing performances with their localized surface plasmon resonance properties.

The possibility of straightforward tuning of the plasmonic properties of metal nanostructures via galvanic replacement has been reported extensively [49, 61, 66, 69, 115, 174, 226, 227]. The galvanic replacement offers a playground of plasmonic nanoparticles across the visible and near infrared regions. Hollow nanostructures exhibits a mechanism called plasmon hybridization, coupling of the surface plasmons of the inner and outer surfaces [61, 63, 66, 67, 116]. In this chapter, we intend to characterize this phenomena with nanometer resolution EELS mapping of hollow AuAg nanoboxes and nanoframes for the first time in literature.

Thanks to the increased surface areas, plasmon hybridization and homogeneous distribution of plasmon fields, hollow nanostructures are known to have better sensing properties than their solid counterparts [67, 126, 140, 141]. After presenting the experimental and simulation results on the local plasmonic properties of hollow AuAg nanostructures by EELS and BEM, we compare the sensitivity of single-walled AuAg nanoboxes and solid Au nanoparticles against bovine serum albumin (BSA) and correlate the sensing results with the experimentally obtained localized surface plasmon resonances.

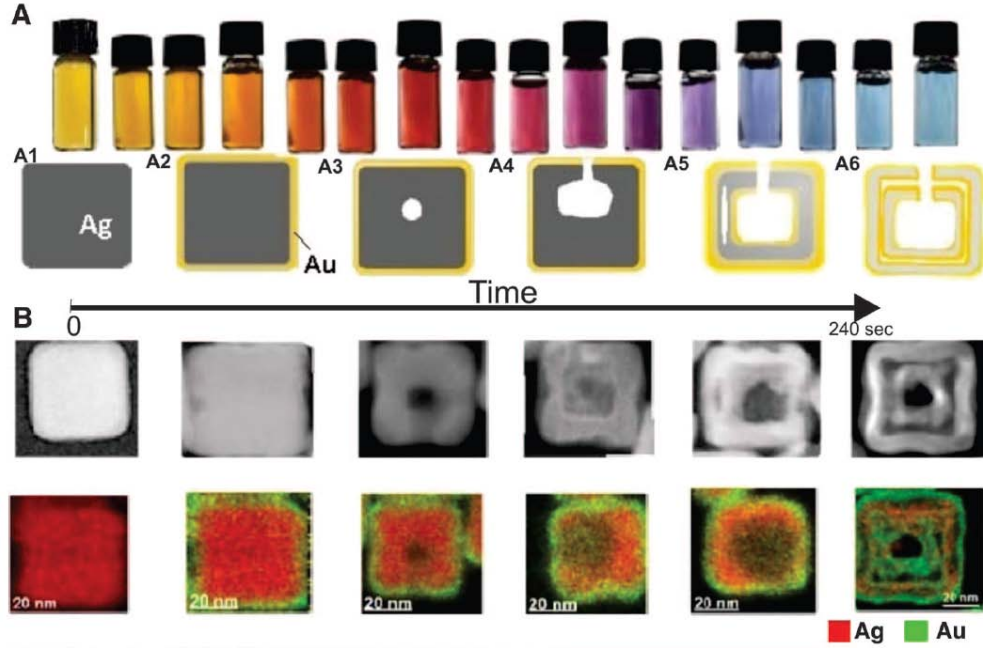


FIGURE 3.1: A. Optical and structural evolution of Ag nanocubes to double-walled AuAg nanobox. B. HAADF STEM micrographs and EDX maps of different stages of the evolution in A (adopted from [69]).

The AuAg nanostructures were synthesized through sequential galvanic replacement and Kirkendall growth at room temperature[69] using Ag nanocubes as templates. Ag nanocubes were synthesized by a modified polyol method[228]. The preparation of AuAg nanoboxes at room temperature comprised the steps of: i) adding cetylammmonium bromide and ascorbic acid into aqueous medium comprising Ag nanocubes, ii) adding various amounts of 0.1mM HAuCl_4 with a flow rate of $25 \mu\text{L}/\text{min}$, and iii) isolating the synthesized nanoboxes by centrifuging and re-dispersing in water or ethanol. The straightforward morphological evolution from solid nanocubes to single-walled nanoboxes is due to the increasing extend of galvanic exchange between Ag and Au, whereas the synthesis of nanoframes and double-walled nanoboxes were made possible by slightly modifying the synthesis procedure[69]. Figure 3.1A shows the optical evolution by the reflected color of the solutions and schematical structural evolution of Ag nanocubes to double-walled AuAg nanoboxes with the addition of Au. HAADF STEM micrographs and their

corresponding EDX maps of different steps of the evolution are presented in Figure 3.1B [69].

Fig. 3.2 shows the HRTEM micrograph obtained from a double-walled AuAg nanobox and details of the red, green and blue squared regions along with their corresponding power spectra (FFTs). As seen in this figure, a nanostructure as complex as a multi-walled nanobox preserves the single crystallinity of the initial Ag nanocubes which were used as templates for the synthesis. FFTs of these regions suggests that the nanobox has a face centered cubic phase and visualized along its [001] zone axis, however, it is hard to distinguish between Ag and Au phases (or their alloys) since they have quite similar lattice parameters ($a_{Au} = 0.4079$ nm, $a_{Ag} = 0.4085$ nm).

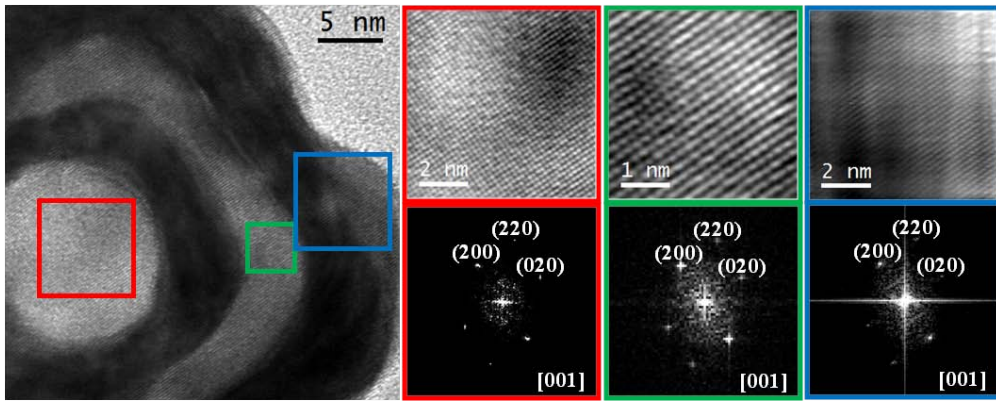


FIGURE 3.2: HRTEM micrograph of a double-walled AuAg nanobox showing the single crystalline structure of the nanobox. Details of the red, green and blue squared regions and their corresponding power spectra are also presented.

After giving a general idea about the structural features of the nanostructures, we continue with the characterization of plasmonic properties of an Ag cube, an Ag@Au core-shell nanocube, a pinholed AuAg nanobox, a single-walled AuAg nanoboxes, an AuAg nanoframe and a double-walled AuAg nanobox by EELS in a monochromated STEM with sub-eV energy resolutions and nanometer spatial resolutions. The detailed discussion of the LSPR properties of each nanostructure are provided in the following, where we compare the results of different processing techniques such as Gaussian fitting, independent component analysis (ICA) by a combination of principal component analysis (PCA) and blind source separation (BSS) [271–273] in HyperSpy multidimensional data analysis toolbox [268] and spectral unmixing (SU) by using vertex component analysis (VCA) [274, 275, 277].

3.2 Ag nanocube

3.2.1 Local plasmonic properties

Figure 3.3A shows the HAADF STEM micrograph of the investigated Ag nanocube which is ~ 55 nm in size and has rounded corners. Selected area EEL spectra of the upper left corner, upper edge/face and center of the nanocube are shown in Fig. 3.3B, which are sum of background subtracted EEL spectra over an area of 5 pixel by 5 pixel (~ 7 nm by 7 nm). Main plasmon peaks are located at ~ 2.6 eV and ~ 3.4 eV for the corner of the nanocube, as seen from the EEL spectrum shown in black in Fig. 3.3B. It should be stressed here that the present peaks are quite wide and may contain some additional "plasmon modes" with lower intensities. The EEL spectrum obtained from the upper edge/face also reveals similar shape with the peaks being located at slightly higher energies compared to those for the corner, where the main peak is located at ~ 3.5 eV and two other peaks are visible at ~ 2.6 eV and ~ 3.1 eV (shown in green in Fig. 3.3B). The EEL spectrum obtained from the "bulk" of the nanocube has lower intensities compared to the outside of the nanocube and it is multiplied by 10 in order to have better comparison with the EEL spectra obtained from the corner and the edge, which reveals the presence of a peak located at ~ 3.8 eV, very well-known bulk plasmon resonance of Ag, in addition to a small peak at ~ 3.1 eV.

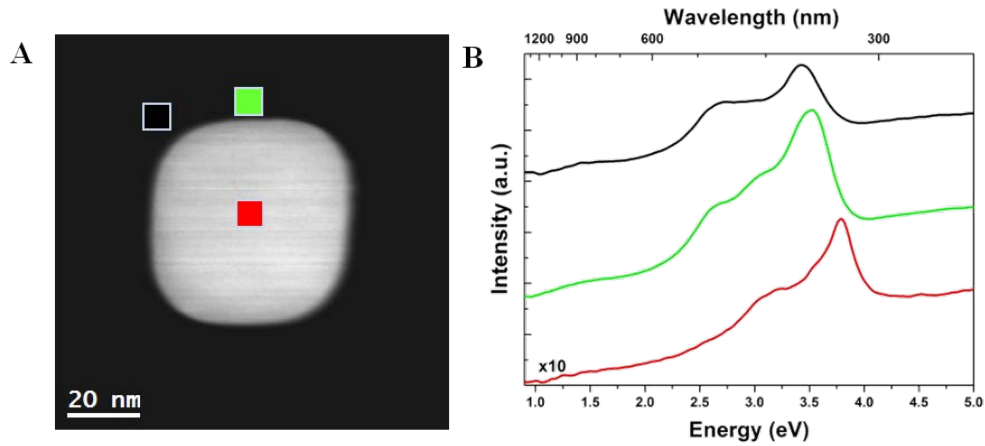


FIGURE 3.3: A. HAADF STEM micrograph of a 55 nm Ag nanocube with rounded corners. B. Selected area EEL spectra of the upper left corner, upper edge/face and center (areas are indicated in HAADF STEM micrograph, which are 5 pixel by 5 pixel)

3.2.2 Processing of plasmonic properties

As mentioned above, we process the EELS data of the Ag nanocube by using different approaches of Gaussian fitting, independent component analysis (ICA) by blind source

separation (BSS) and vertex component analysis (VCA). In the following we present localized surface plasmon resonances of the Ag nanocube obtained by these three routines and compare the results.

Fig. 3.4 shows the plasmon energy (A) and intensity (B) maps obtained by fitting a Gaussian between the given energy ranges. We could map 4 different LSPR "modes" corresponding to the resonances from the corners (energy map between 2.4 - 3.0 eV in Fig. 3.4A), the edges/faces (energy maps between 2.7 - 3.3 eV and 3.2 - 3.7 eV) and the bulk of the Ag nanocube (energy map between 3.6 - 3.9 eV). It is evident from the energy maps of the LSPR modes corresponding to the corners (between 2.4 and 3.0 eV) and the edges/faces (between 3.2 and 3.7) that their corresponding plasmon resonances are not well separated from one another and have interacting contributions. In other words, the plasmon energy map that reveals the corner resonances at ~ 2.7 eV also shows that the edges have a plasmon resonance at ~ 2.6 eV (green regions in the energy map between 2.4 and 3.0 eV in 3.4A), which was also revealed in 3.3B. Such a behavior is probably due to the fact that the investigated Ag nanocube has rounded corners, as it will be discussed in more detail in the following on the basis of BEM simulations.

Notice that the presented intensity maps in Fig. 3.4B are more or less similar to one another and does not correlate with the corresponding plasmon energy maps due to the fact that the tail of the Gaussian fitting extend more than the fitted values (which can be limited in the case of the plasmon energy maps, because the energy range is simply the contrast value in these maps) and cause the normalization of the plasmon intensity maps over a wider energy range and, therefore, giving similar intensity maps since the distribution of maximum and minimum plasmon intensities is similar around the Ag nanocube. Even the plasmon intensity map of the bulk mode is similar to the maps of the other surface resonances, for which we have limited the energy range strictly to the range of the Gaussian fitting with a MatlabTM code to obtain a "reasonable" plasmon intensity map as the one shown in Fig. 3.4B. As can be seen from the figure, the color-code and the scale bar is different for this figure simply because the "temperature" color scale we have used for the other maps is not adopted to the MatlabTM.

For a second approach to process the obtained low-loss EELS spectrum images, we have used a multivariate component analysis based technique, namely independent component analysis based on the combination of principal component analysis (PCA) and blind source separation (BSS) in Hyperspy. As explained in the experimental details, this technique decomposes the SI into two matrices which are factors and loading matrices that contain the spectral signature and the weighting of the factor components, respectively. In the first step, we use the weighed PCA, in which the dataset is described

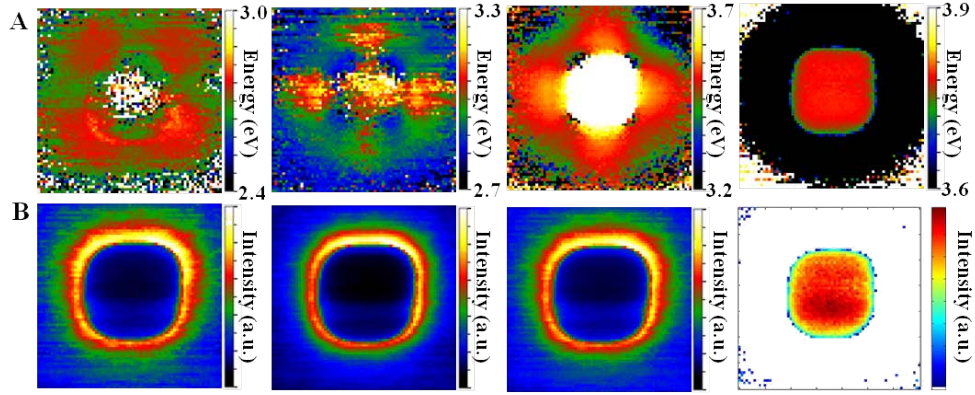


FIGURE 3.4: A. Plasmon energy maps of the Ag nanocube, obtained by fitting a Gaussian between the energy ranges of 2.4 - 3.0 eV, 2.7 - 3.3 eV, 3.2 - 3.7 eV and 3.6 - 3.9 eV and B. their corresponding plasmon intensity maps. Notice that the colorcode and the scale is different for the intensity map of the bulk mode, where white pixels are the pixels with lowest intensity.

as a weighted sum of finite number of components and Poissonian noise that are separated according to their variances. Application of weighted PCA allows us to increase the signal-to-noise ratio by reconstructing the dataset only with the higher variance components and therefore, minimizing the noise contribution. Moreover, it provides the linearity of the data and thereby we can apply BSS in order to obtain independent spectral components.

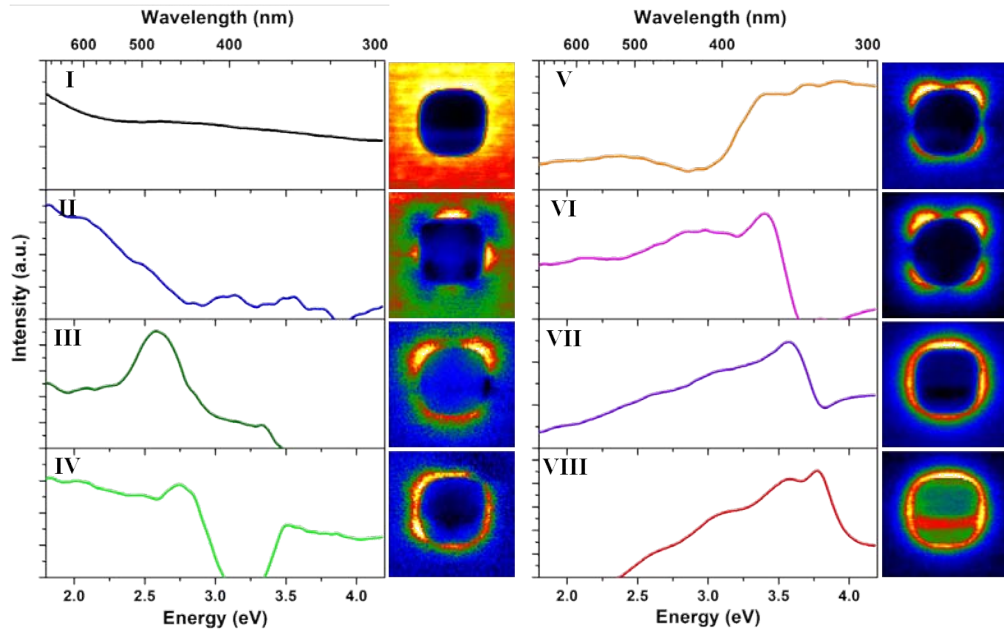


FIGURE 3.5: Blind source separation (BSS) analysis of the Ag nanocube: Spectra of the 8 components and their corresponding abundance maps.

Figure 3.5 shows the spectra of 8 components obtained by using the blind source separation (BSS) algorithm and their corresponding abundance maps. As seen in this figure,

spectra of component I and component II suggest that these components are mainly due to the background contribution, whereas, the abundance map of the component II suggest some additional contribution from the edges. In general, it can be commented that the individual spectra presented in this figure are not well isolated and may result in some "outer" contributions. The component III shows a peak located at ~ 2.6 eV, which mainly corresponds to a LSPR mode present in the upper corners. With its energy lower than the other corner LSPR modes (components V and VI), this mode can be labeled as the proximal corner mode [90]. The fact that it is not the same for each corner can be related to the structure of the investigated Ag nanocube with its rounded corners. One needs to conduct 3D analysis on such nanostructures in order to have a full understanding of their LSPR properties. Components IV and V do not reveal proper peaks, therefore, their maps are also can not be related to the previously reported LSPR modes of Ag nanocubes [90, 216]. Component VI reveals the presence of a main peak at ~ 3.4 eV which is related to the corner LSPR modes as showed in its corresponding abundance map. The face (~ 3.6 eV) and bulk (~ 3.8 eV) modes, which are also revealed by the Gaussian fitting (Fig. 3.4), are shown in the components VII and VIII, respectively. One can notice that since the obtained spectrum of the component VIII for the bulk resonance has a "tail" along the lower energies with several shoulder peaks, its corresponding map suggests that this mode is present at the surrounding of the Ag nanocube which was also the case for the regular Gaussian fitting as discussed above.

The third approach we have used to process the EELS data is based on spectral unmixing (SU) technique using vertex component analysis (VCA). Fig. 3.6 shows the spectra of 8 components and their corresponding abundance maps obtained by using VCA. Component I shows a peak at 2.6 eV which is present at the upper corners. This component is equivalent to the component III of the Fig. 3.5. Component II, which has the main peak at ~ 2.8 eV, is related to the corners as well as some modes related to the edges which show lower intensities. The plasmon resonance at ~ 3.0 eV (component III) seems to be present all around the nanocube, which is consistent with the selected area EEL spectra of the Ag nanocube presented in Fig. 3.3. Components IV and V show the corner LSPR modes located at 3.3 eV and ~ 3.45 eV, respectively. The well-known face mode at ~ 3.6 eV and the bulk mode at 3.8 eV for the Ag nanocubes [90, 216] are shown in components VI and VII, respectively. Finally, component VIII is due to background contributions. By comparing Fig. 3.5 and Fig. 3.6, one can see that the spectra of the components are better defined for the VCA processing than those for the BSS, therefore, it can be suggested that the VCA routine produces more reliable abundance maps for the components [274].

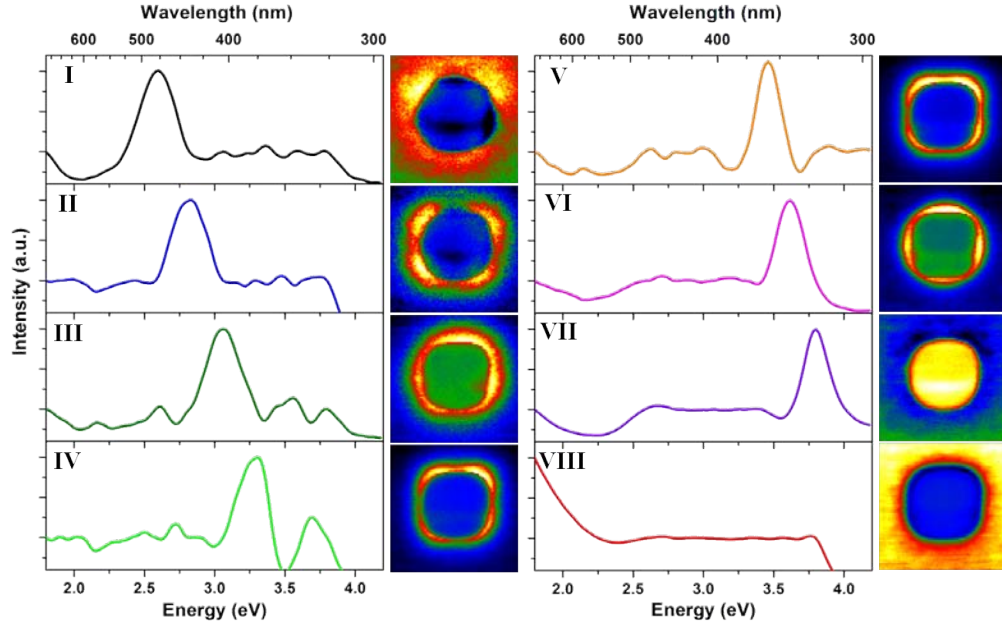


FIGURE 3.6: Vertex component analysis (VCA) of the Ag nanocube: Spectra of the 8 components and their corresponding abundance maps.

TABLE 3.1: Comparison of the plasmon components obtained by Gaussian fitting, BSS and VCA routines for the Ag nanocube.

	Gaussian fitting ^a	BSS	VCA
1st component	2.4-3.0 eV	~2.6 eV	2.6 eV
2nd component	2.7-3.3 eV	~3.4 eV	~2.8 eV
3rd component	3.2-3.7 eV	~3.6 eV	~3.0 eV
4th component	3.6-3.9 eV	~3.8 eV	3.3 eV
5th component			~3.45 eV
6th component			~3.6 eV
7th component			~3.8 eV

^aNote that the energy values of the components for the Gaussian fitting are given as ranges of energies, which indicates the range of peak fitting.

Since we have mentioned about the presence of many different modes obtained by three independent processing routines, it is convenient to compare all the modes obtained by Gaussian fitting, BSS and VCA in a table. Table 3.1 shows the energy values of different components obtained by the different processing algorithms. It should be noted here that the energy values of the components for the Gaussian fitting are given as ranges of energies, which indicated the range of peak fitting. Another note should be underlined for the components obtained by BSS analysis. As shown in Fig. 3.5, 8 different components with, to some extent, physical meaning are generated by using the BSS analysis on the EELS data of the Ag nanocube. Although it is expected to have only one component related to the background contributions during such a multivariate component analysis

routine, several other components are considered as background contributions due to the lack of a dominant peak presence. Thus, we present in this table only 4 of these 8 components, in which we could define the energy values. On the other hand, 7 of 8 components, excluding the component related to the background contribution, obtained by VCA (Fig. 3.6) are presented in Table 3.1.

3.2.3 Boundary element method (BEM) simulations

In the following, we present the simulation studies of LSPRs on Ag nanocube obtained by using the boundary element method (BEM) developed by García de Abajo and Howie [281]. In particular, we have used the implementation of the BEM method in the MNPBEM Matlab toolbox developed by U. Hohenester (<http://physik.uni-graz.at/mnpbem/>) [282]. Compared to other methods such as the dipole-dipole approximation (DDA), the BEM method can easily deal with electron trajectories penetrating into the particle and it is computationally more effective since it discretizes the surface and not the whole particle volume. The differences between these simulation methodologies are discussed in more detail in the experimental details section. We have conducted systematic BEM simulations in order to investigate the effects of substrate, corner rounding and experimental broadening on the plasmonic properties of Ag nanocubes.

Fig. 3.7 shows the results obtained by BEM simulation on a 50 nm Ag nanocube in vacuum. These simulation results present the local plasmon resonances of the corner, edge and center and plasmon maps for the resonances observed in the simulated EEL spectra. Fig. 3.7A shows the BEM simulated EEL spectra of the corner, edge and center of the Ag nanocube, indicating the presence of several plasmon resonances, the lowest energy being at ~ 3 eV. The plasmon resonance energies are higher than those observed experimentally (see Fig. 3.3). The reasons for such difference, i.e. the presence of a substrate and the shape of the nanocube, are discussed in the following. The simulated EEL spectra of the corner reveals the presence of 4 different peaks, the main peak being located at ~ 3.1 eV. Likewise, the simulated EEL spectra of the edge also reveals the presence of at least 4 different peaks, two of them are located at 3.4 eV and 3.7 eV. The simulated EEL spectra of the center reveals the presence of two main peaks at 3.7 eV and 3.8 eV with some additional small peaks at lower energies. Fig. 3.7B shows the corresponding plasmon maps for the 6 different peaks shown in Fig. 3.7A, that are located at 2.99 eV, 3.07 eV, 3.17 eV, 3.40 eV, 3.70 eV and 3.80 eV. The first two maps at 2.99 eV and 3.07 eV shows that the plasmons with these energy values are located at the corners of the Ag nanocube, whereas the mode at 3.17 eV shows the main excitations from the corner along with some contributions at the edges. The LSPR mode at 3.40 eV is the main edge mode with some contributions at the corners. As also seen in this

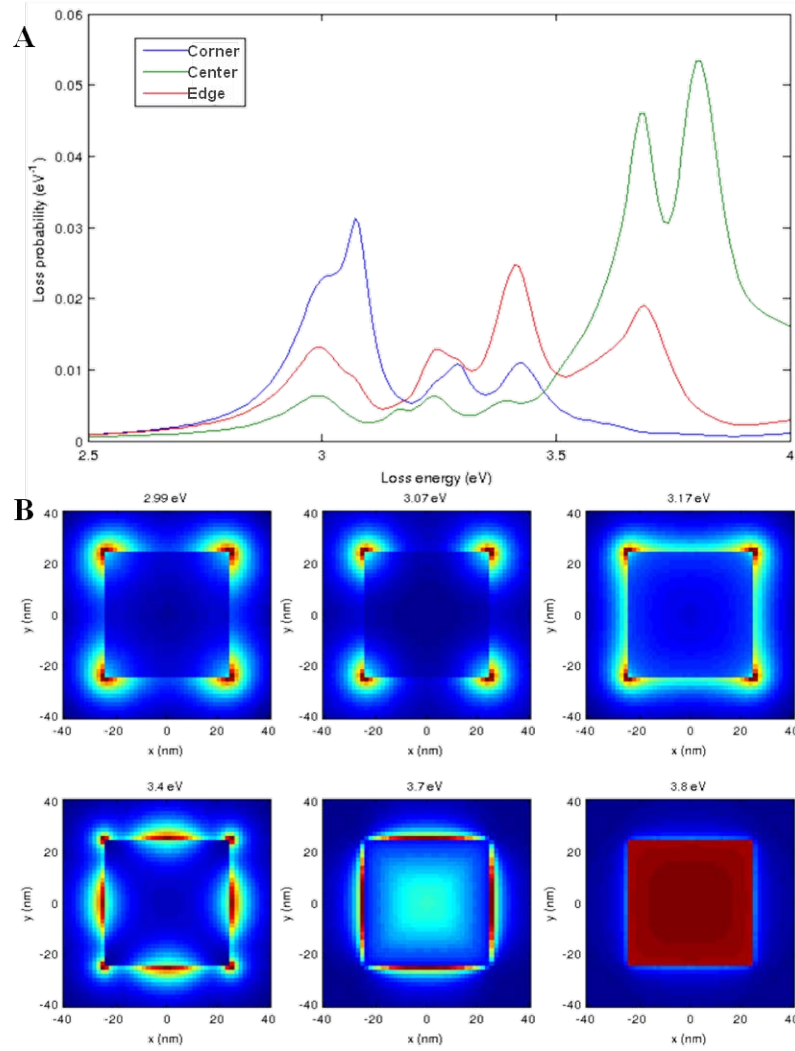


FIGURE 3.7: BEM simulations of a 50 nm Ag nanocube in vacuum: A. Simulated selected area EEL spectra of the Ag nanocube from the corner, edge and center. B. Simulated plasmon maps for LSPRs at 2.99 eV, 3.07 eV, 3.17 eV, 3.40 eV, 3.70 eV and 3.80 eV.

figure, face LSPR mode of the Ag nanocube is located at 3.70 eV and the "bulk" mode is at 3.8 eV.

Fig. 3.8 shows charge distributions and field maps of the LSPR modes presented in Fig. 3.7. The maps presented in this figure are mainly obtained by a beam excitation at the edge except the one at 3.07 eV, which is obtained by a corner beam, and the one at 3.80 eV (bulk mode), which is obtained by a center beam. The corner mode at 2.99 eV is a bright mode which is evident from the charge distribution map showing equal charges at the corners of the same face. On the other hand, the corner mode at 3.07 eV, which is excited by a corner beam, is a dark mode and shows the opposite charges at the corners of the same face. The corner-edge mode at 3.17 eV shows the same charges at the corners, which are opposite of the ones located at the edges. Edge and face modes at

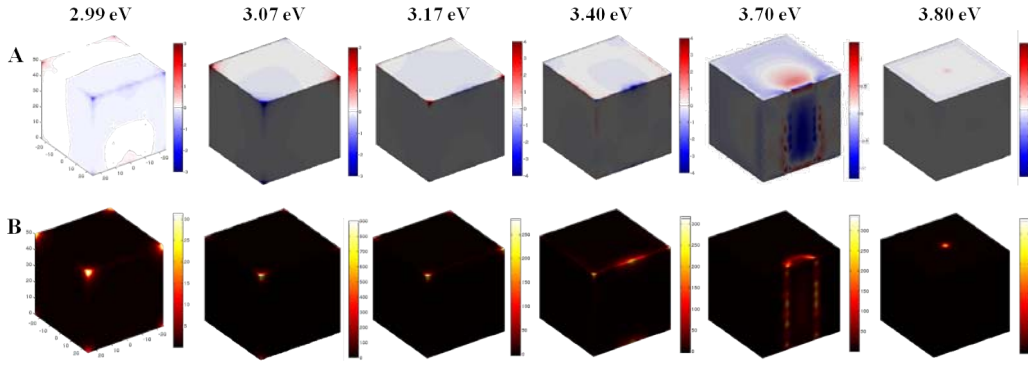


FIGURE 3.8: BEM simulations of Ag nanocube: Charge distribution maps (A) and their corresponding field maps (B) of different plasmon modes located at 2.99 eV, 3.07 eV, 3.17 eV, 3.40 eV, 3.70 eV and 3.80 eV. Maps are mostly obtained by a beam excitation at the edge except the one at 3.07 eV, which is obtained by a corner beam excitation, and the one at 3.80 eV (bulk mode), which is obtained by a center beam excitation.

3.40 and 3.70 eV show charge concentrations at the edges and faces, respectively. It can also be seen in this figure that the excitation with the center beam does not generate any surface charges and the plasmon is excited in the volume, hence it is called the bulk mode.

Above presented simulations are conducted on perfect nanocubes with sharp corners, however, chemically synthesized nanocubes usually have smooth corners, which may effect the LSPR modes of the nanocube [104, 292]. Since the experimentally investigated Ag nanocube has rounded corners (Fig. 3.3), we discuss the effects of corner rounding on the LSPR properties of the Ag nanocubes in the following. In Fig. 3.9, BEM simulations of 50 nm Ag nanocubes with sharp corners and corners rounded by radii of 2 nm, 5 nm and 10 nm are presented. As seen in this figure, corner LSPR modes shift to higher energies and their intensity quench with increasing roundness. Moreover, as the nanocube gets rounder, the edge and face modes merge together towards a single dipolar mode similar to that of spheroidal nanoparticles.

Another issue to be considered other than shape effects is the effect of a substrate on the plasmonic properties. It is well-known that the presence of a substrate changes the local dielectric environment and modifies the conditions for the excitation of the plasmon modes [87, 90, 91, 216]. Interaction with the substrate breaks the degeneracy of the plasmon modes into proximal (in contact with the substrate) and distal (opposite site of the substrate) modes [90, 91]. Therefore, the presence of a 15 nm thick Si_3N_4 substrate affects the plasmon modes generated by the Ag and AuAg nanostructures in the present study. So far, we have shown the simulations on Ag nanocubes in vacuum, meaning that the sample is not in contact with any substrate, however, it is not the case for the experimental results and one needs to consider the effects of the substrate in

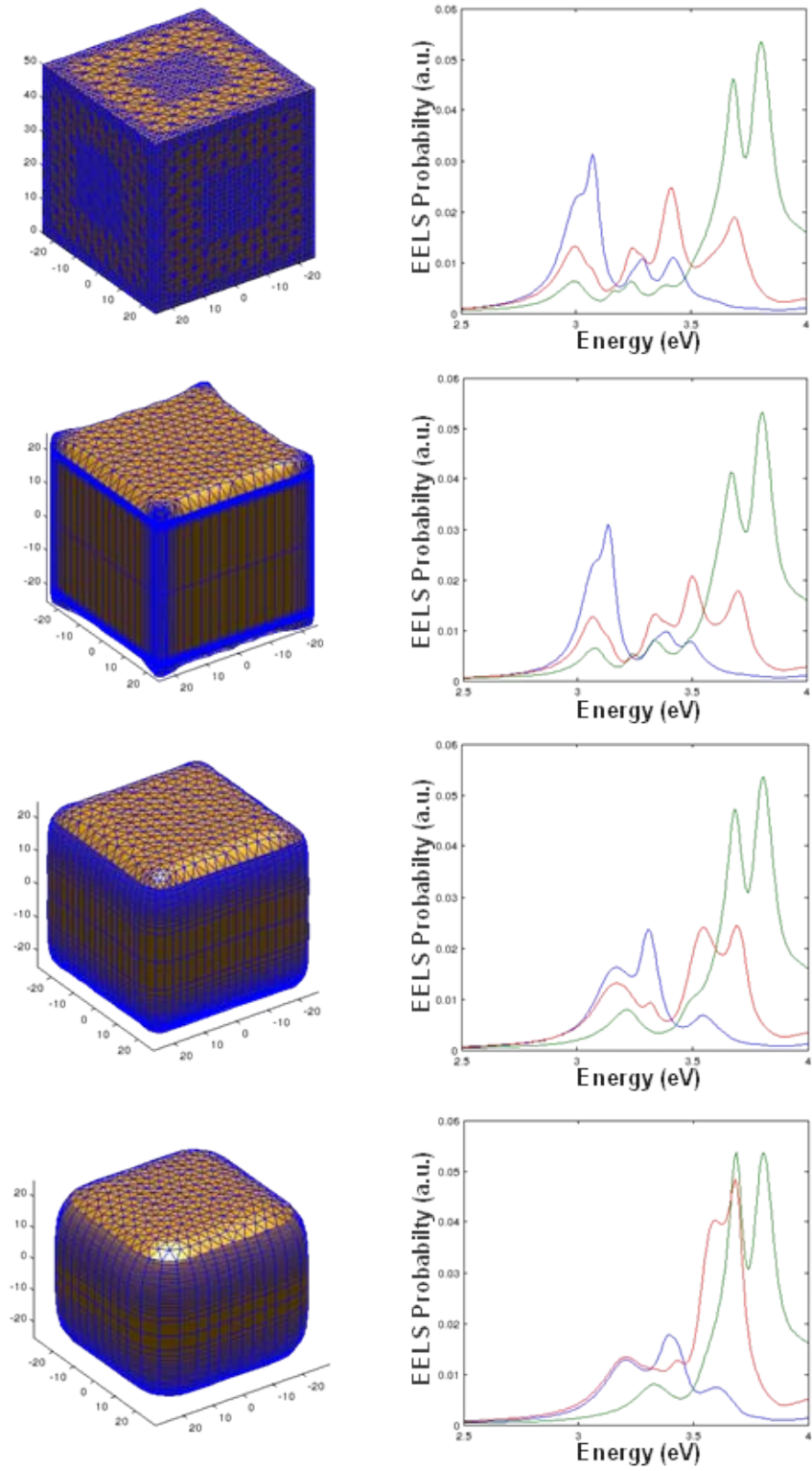


FIGURE 3.9: Effect of rounded corners on the LSPR properties of Ag nanocubes: Nanocube with perfect corners and nanocubes with rounded corners with radii of 2 nm, 5 nm and 10 nm. Corner excitations are in blue, edge excitations are in red and center excitations are in green for all the EEL spectra presented on the right.

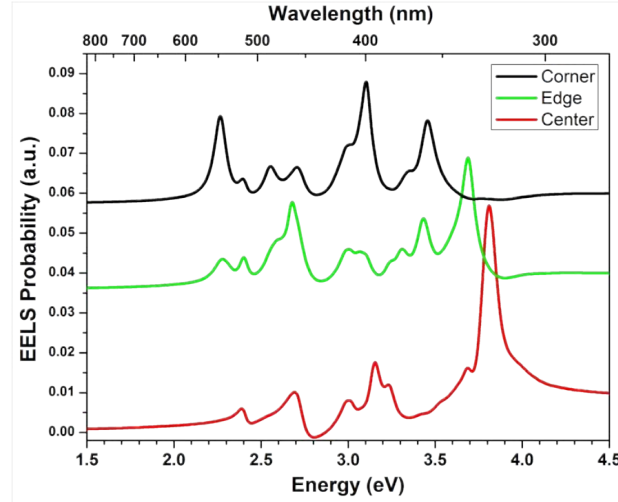


FIGURE 3.10: BEM simulations of a 50 nm Ag nanocube on 15 nm thick Si_3N_4 substrate: Simulated selected area EEL spectra of the Ag nanocube of the corner, edge and center.

order to obtain simulation results that are consistent with the experimental ones. Fig. 3.10 shows the BEM simulated EEL spectra from the corner, edge and center of a 50 nm Ag nanocube on 15 nm Si_3N_4 substrate. It is clear from this figure that some additional plasmon resonances of the corner and edge modes appear at the Ag nanocube on a substrate (compare with Fig. 3.8) and, in general, plasmon resonances shift to lower energies.

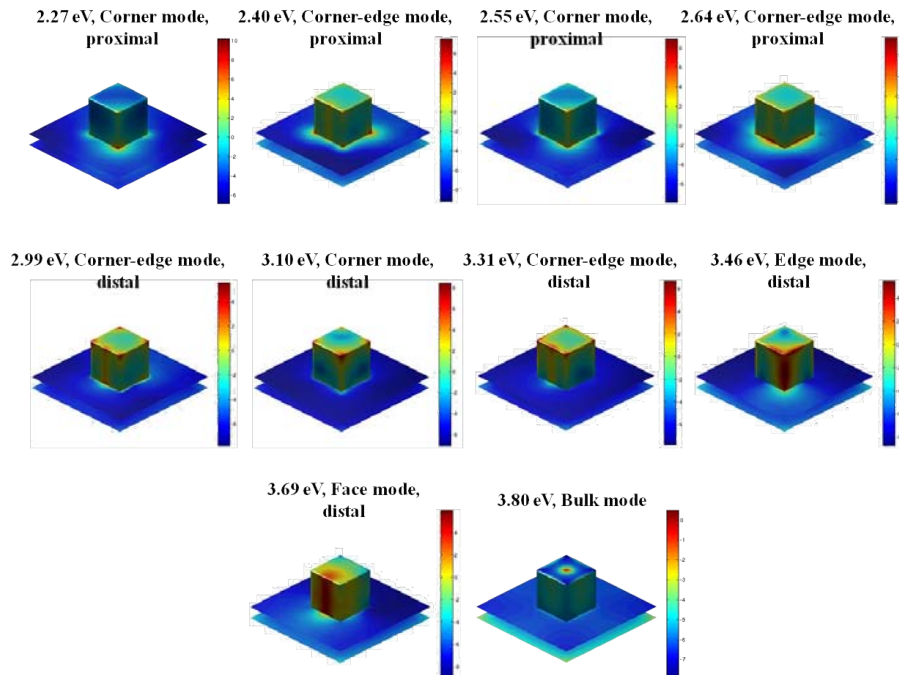


FIGURE 3.11: BEM simulations of a 50 nm Ag nanocube on 15 nm thick Si_3N_4 substrate showing field maps of different proximal and distal plasmon modes.

Fig. 3.11 shows field maps of different proximal and distal plasmon modes in a 50 nm Ag nanocube located on a 15 nm thick Si_3N_4 substrate. As seen in this figure, several corner and corner-edge modes are labeled as proximal and distal modes where there is an energy difference of ~ 0.6 eV between proximal and distal plasmon modes which have the same energy for the nanocubes standing in vacuum (Fig. 3.7). Such simulation results were proven experimentally by Nicoletti et al. [90] where they investigated the 3-dimensional plasmonic properties of a Ag nanocube on a Si_3N_4 substrate and showed the energy shift of different corner and edge modes due to the interaction with the substrate.

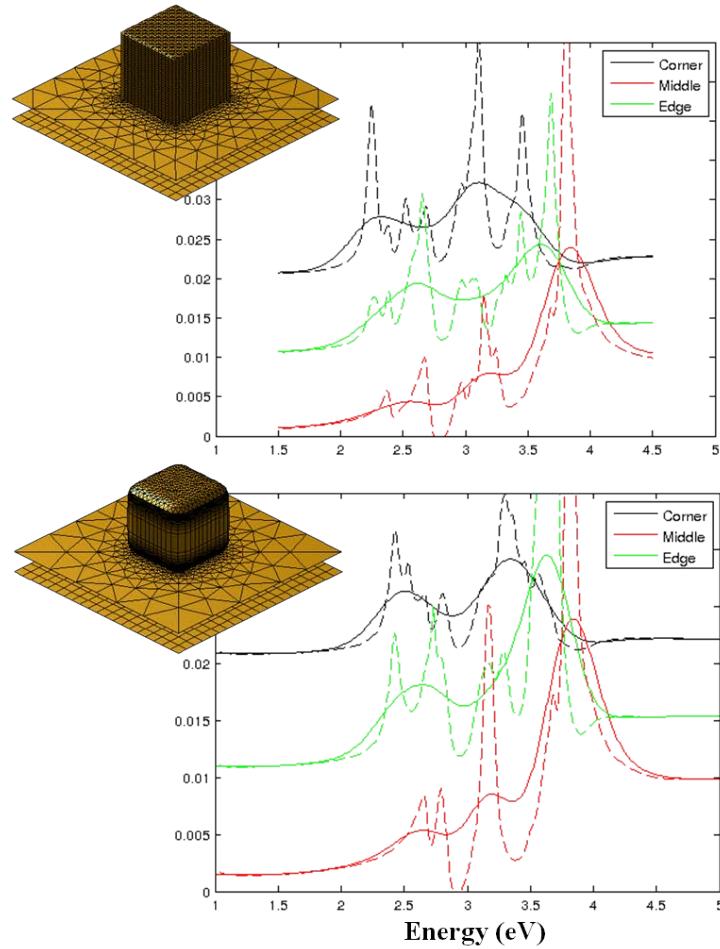


FIGURE 3.12: BEM simulated local plasmon responses of 50 nm Ag nanocubes with sharp corners (upper) and rounded corners (lower) on SiN_x substrate. Dashed lines show the results obtained by BEM simulations and continuous lines show the results of BEM simulations after taking the experimental broadening, i.e. energy resolution, into account.

Fig. 3.12 shows the models and BEM simulated EEL spectra of the 50 nm Ag nanocubes with sharp corners and rounded corners. As discussed above, rounded corners affect the plasmon modes of the Ag nanocubes and experimentally investigated Ag nanocube (Fig. 3.3A) found to have corners rounded with a radius about 15 nm. Therefore, this figure shows the comparison of BEM simulated EEL spectra obtained from 50 nm Ag

nanocubes with sharp corners and corners rounded with a radius of 15 nm. As seen in this figure, also pointed out above, the corner plasmon modes of the rounded nanocube shifts to higher energies compared to those of the nanocube with sharp corners. It is also worth noting that we compare the simulation obtained with no experimental limitations such as energy resolution (dashed lines) and taking the instrumental broadening into account by introducing an energy resolution of 0.2 eV to the BEM simulations (solid lines). The intensities of the plasmon peaks decrease and more importantly several plasmon modes are merged together as the instrumental broadening introduced, which is the case for the experimentally obtained EEL spectra. A perfect fit between the EEL spectra obtained experimentally (Fig. 3.3) and by BEM simulations (Fig. 3.12) is achieved. Fig. 3.13 shows several examples of BEM simulated plasmon maps from Ag nanocubes with rounded corners with a radius of 15 nm. As seen in these figure, the modes are not as confined as the case of sharp nanocubes, where especially the corner modes merge with edge and face modes.

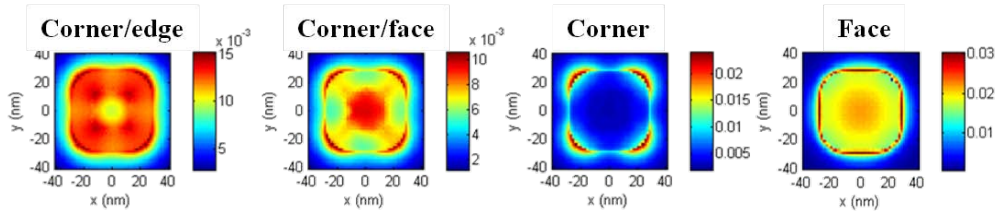


FIGURE 3.13: Selection of BEM simulated plasmon maps obtained from Ag nanocubes with rounded corners, radius = 15 nm, revealing the merging of corner and other modes.

3.3 Ag@Au core-shell nanocube

3.3.1 Local plasmonic properties

Fig. 3.14 shows the HAADF STEM micrograph of a 51 nm Ag@Au core-shell nanocube and selected area EEL spectra of the upper left and upper right corners, upper edge/face and center of the core-shell nanocube. As seen in the EEL spectra presented in Fig. 3.14B, the peaks obtained from the upper left and right corners and the upper edge are quite wide and may contain several LSPR modes. Main peaks for these locations are at ~ 1.9 eV, especially for the corners, and at ~ 2.6 eV with some other small peaks appearing around 3 eV and 3.6 eV. The EEL spectrum obtained from the center of the Ag@Au core-shell nanocube reveals the presence of a peak at 3.8 eV, which corresponds to the bulk plasmon resonance of Ag.

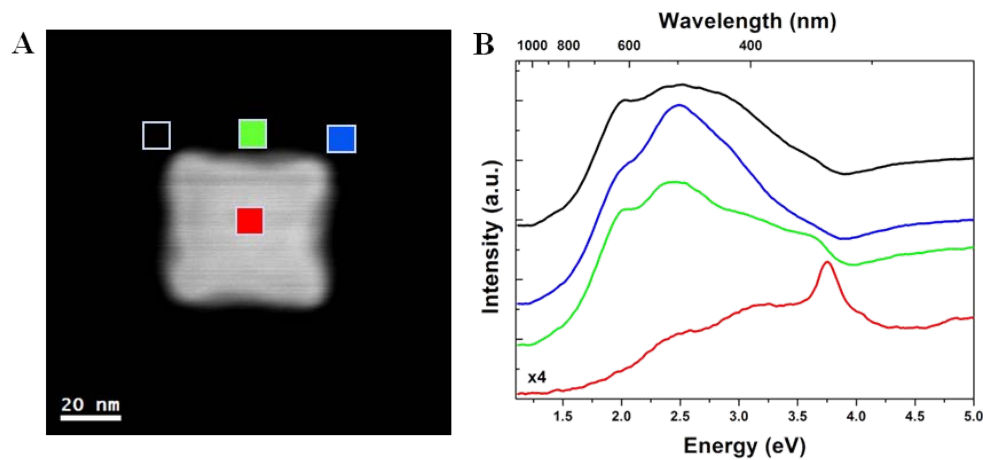


FIGURE 3.14: A. HAADF STEM micrograph of a 51 nm Ag@Au core-shell nanocube. B. Selected area EEL spectra of the upper left and upper right corners, upper edge and center (areas are indicated in HAADF STEM micrograph, which are 5 pixel by 5 pixel).

3.3.2 Processing of plasmonic properties

Similar to the above presented processing of EELS-SI obtained from the Ag nanocube, we present the EELS data obtained from the Ag@Au core-shell nanocube processed using the same 3 techniques of the Gaussian fitting, BSS and VCA. Fig. 3.15 shows the plasmon energy (A) and intensity (B) maps of the Ag@Au core-shell nanocube obtained by fitting a Gaussian between the energy ranges of 1.8 - 2.6 eV, 2.3 - 3.3 eV, 3.2 - 3.7 eV and 3.5 - 3.9 eV. First map in 3.15 corresponds to the peak located at ~ 1.9 eV and, as seen in the plasmon energy map, it is distributed around the nanocube with no specific location such as corners or edges. For the second map, we have fitted a Gaussian to the energy range between 2.3 and 3.3 eV for the wide peak present in the

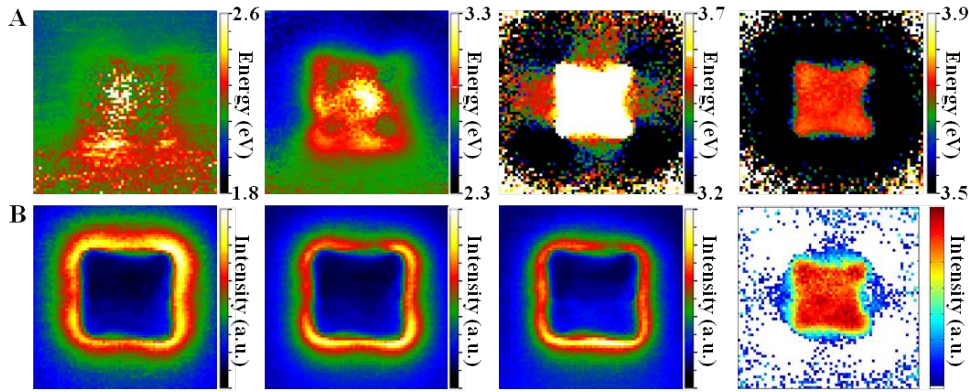


FIGURE 3.15: A. Plasmon energy maps of the Ag@Au core-shell nanocube, obtained by fitting a Gaussian between the energy ranges of 1.8 - 2.6 eV, 2.3 - 3.3 eV, 3.2 - 3.7 eV and 3.5 - 3.9 eV and B. their corresponding plasmon intensity maps. White pixels in the energy maps are out of fitting parameters. Notice that the plasmon intensity map between 3.5 and 3.9 eV has a different color code, where white pixels are the pixels with lowest intensity.

EEL spectra obtained from the upper corners and the upper edge (Fig. 3.14B). As seen in this plasmon energy map, the upper right corner has a lower LSPR energy compared to the other corners. Such a behavior can be explained by structural changes, which is already evident in the plasmon energy map of the bulk plasmon mode of Ag mapped between 3.6 and 3.9 eV, where it is observed that the upper right corner is corroded more than the other corners and it is sharper. In addition to these LSPR modes, it was also possible to map the face mode of Ag at ~ 3.6 eV under a shell of Au (or AuAg alloy). Plasmon intensity maps for the Ag@Au core-shell nanocube are similar to one another up to some extent and the corresponding plasmon intensity map for the bulk plasmon resonance of Ag is obtained using the MatlabTM code as discussed for the case of the Ag nanocube.

One can obtain some additional information about the chemistry of the Ag@Au core-shell nanocube by looking at the plasmon maps presented in Fig. 3.15. As discussed above, the galvanic exchange among the nanocube has not taken place homogeneously, resulting in the upper right corner being sharper than the others, which obviously affects the distribution of LSPRs throughout the nanocube. In Fig. 3.16, a composite map of the HAADF STEM micrograph obtained during the EELS acquisition and the plasmon energy map for the bulk plasmon mode of Ag is shown in order to reveal the thickness of the Au (or AuAg alloy) shell, which is found to be ~ 5 nm around the nanocube and it is thicker at the upper and right edges (7.7 nm at the right edge).

After having a first look to the structure and local distribution of LSPRs of the Ag@Au core-shell nanocube, we present the BSS analysis showing the spectra of 6 components and their corresponding abundance maps in Fig. 3.17. It should be noted here that

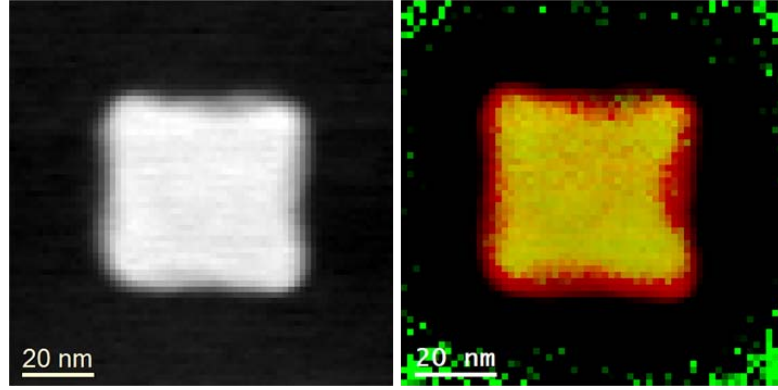


FIGURE 3.16: HAADF STEM micrograph of the Ag@Au core-shell nanocube obtained simultaneously during EELS acquisition and its colored composite with the plasmon energy map for the bulk plasmon mode of Ag. Pixel size, which corresponds to the spatial resolution of the EELS maps, is 1.54 nm.

the BSS analysis is conducted taking 7 components into account but the component corresponding to the background (similar to the component I in Fig. 3.5) is not shown in this figure. First component in the Fig. 3.17 shows a small peak at 1.9 eV, which seems to be only present at the upper part of the Ag@Au core-shell nanocube. The plasmon resonance energy of this component is similar to the peak observed at the upper corners and the upper edge (Fig. 3.14). The component II has a peak at ~ 2.5 eV and its corresponding map reveals that this LSPR mode is a corner mode with some contributions from the edges. It is more intense at the upper right corner compared to the other corners due to the fact that this corner is more corroded than the others, which is discussed above thoroughly. The components III and IV are also corner modes located at 2.8 eV and ~ 2.9 eV, respectively, where the component III is only present at the lower corners and the component IV is present at all corners with the particular situation of being really weak at the upper right corner. The components V and VI are well-known face and bulk plasmon resonances of Ag, respectively. However, since the spectra of the component reveals wide peaks, the modes are not located only at the faces and bulk of the nanocube.

Fig. 3.18 shows the VCA analysis of the EELS-SI obtained from the Ag@Au core-shell nanocube which is done by taking 7 components into account, 5 of them are presented in this figure. The component I shows a peak located at 1.9 eV and it is the same as the one obtained during the BSS analysis (Fig. 3.17), i.e. it is mostly located at the upper part of the nanocube. The component II shows a plasmon resonance at 2.3 eV, which is mostly confined at the upper right corner of the nanocube. The component III is a corner LSPR mode with some contributions from the edges and it shows a plasmon peak at ~ 2.6 eV with a shoulder at ~ 2.7 eV. Another corner LSPR mode, which has an energy of ~ 2.9 eV and present at the lower corners more intensely, is revealed in the

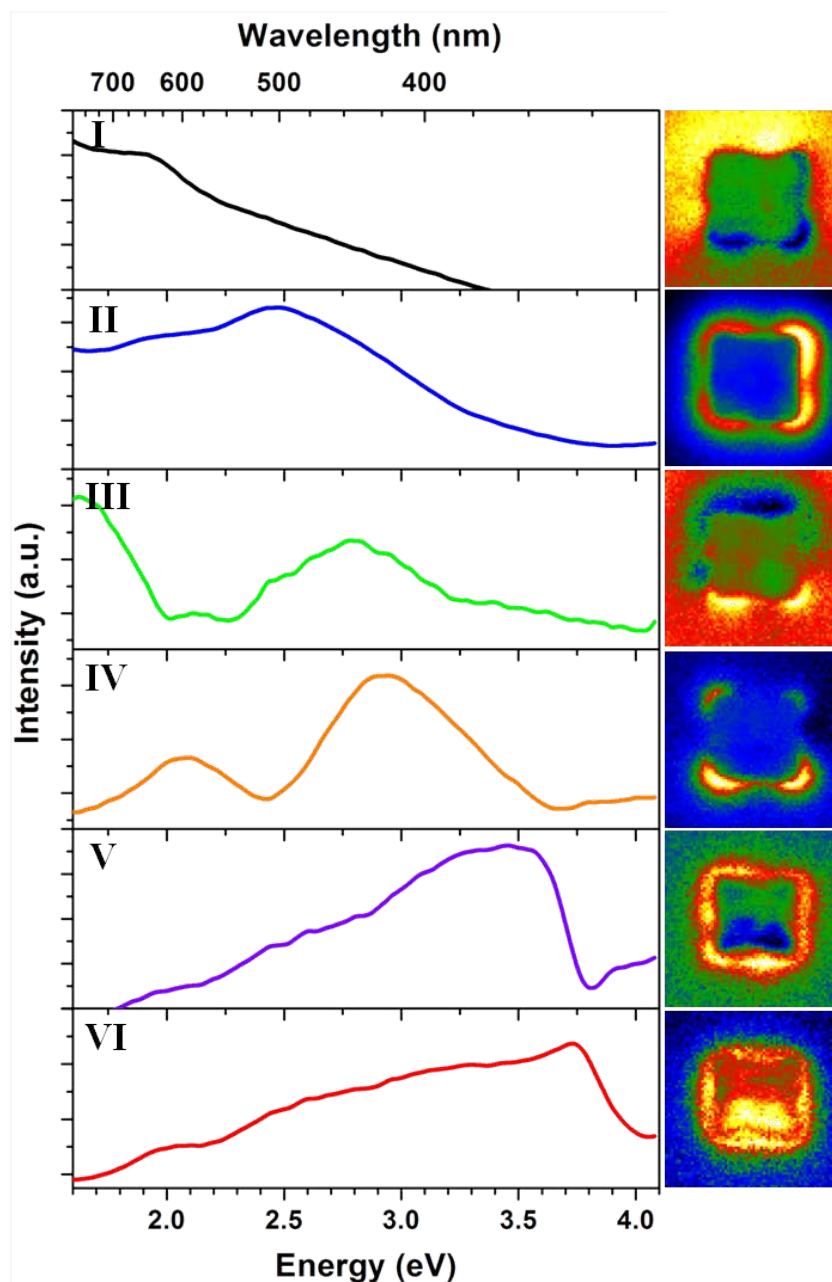


FIGURE 3.17: BSS analysis of the Ag@Au core-shell nanocube: Spectra of the 5 components and their corresponding abundance maps.

component IV. A well separated/confined component is obtained for the bulk plasmon resonance of Ag (component V) and its corresponding abundance maps reveals quite similar distribution as the Gaussian processing (Fig. 3.15). It should be noted here that a component revealing a LSPR mode located at ~ 3.6 eV, face LSPR mode of Ag nanocubes, is obtained during the VCA analysis, however its spectrum was quite irregular and its abundance map was too noisy, so we have chosen to exclude it from this figure. Similar to the above presented processing results for the Ag nanocube, the VCA analysis provided better defined components and plasmon distribution maps than

those obtained by using BSS analysis.

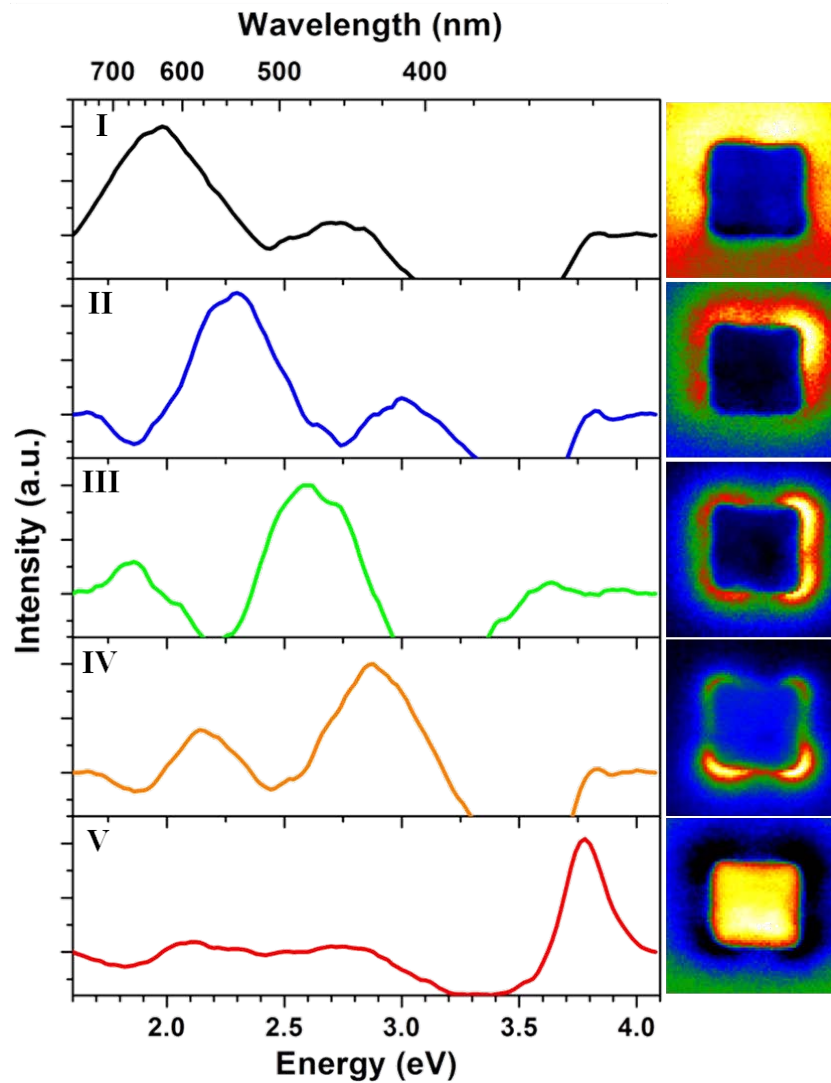


FIGURE 3.18: VCA analysis of the Ag@Au core-shell nanocube: Spectra of the 5 components and their corresponding abundance maps.

Similar to the case for the above presented Ag nanocube, we have mentioned about the presence of many different modes obtained by the three different processing routines. Table 3.2 shows the energy values of different components obtained by different processing algorithms. It should be noted here that the energy values of the components for the Gaussian fitting are given as ranges of energies, which indicated the range of peak fitting. Energy values of the dominant peaks in the 6 different components obtained by BSS and 5 different components obtained by VCA are listed in this table.

TABLE 3.2: Comparison of the plasmon components obtained by Gaussian fitting, BSS and VCA routines for the Ag@Au core-shell nanocube.

	Gaussian fitting	BSS	VCA
1st component	1.8-2.6 eV	1.9 eV	1.9 eV
2nd component	2.3-3.3 eV	~2.5 eV	2.3 eV
3rd component	3.2-3.7 eV	2.8 eV	~2.6 eV
4th component	3.5-3.9 eV	~2.9 eV	~2.9 eV
5th component		~3.5 eV	~3.75 eV
6th component		~3.7 eV	

3.3.3 Boundary element method (BEM) simulations

The galvanic replacement seems to take place quite un-evenly for the case of the investigated Ag@Au core-shell nanobox as judged by the local variations of the plasmonic properties (see Fig. 3.16). Since we do not know the exact morphology and compositions in 3D, we simulate a rather general Ag@Au core-shell nanocube for the sake of a discussion on the effects of Au shell presence on the plasmonic properties of Ag nanocube. As it has not been introduced in this study, we start simulating the Au nanocube in order to better elucidate contributions of Au related plasmon modes in the Ag@Au core-shell case.

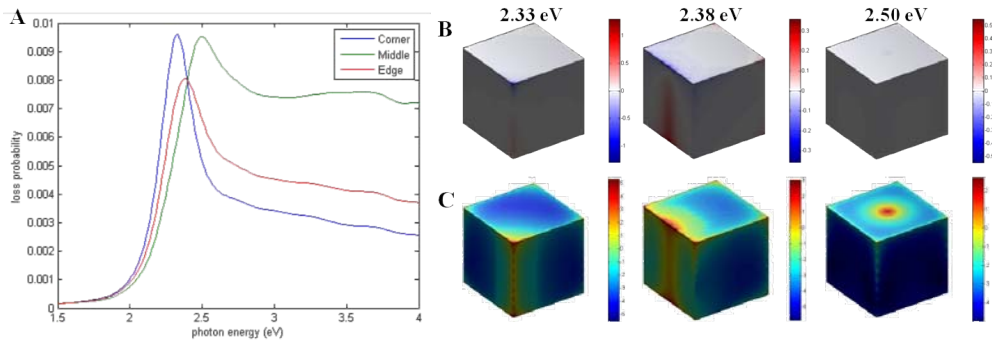


FIGURE 3.19: A. BEM simulated local EEL spectra of a 50 nm Au nanocube B. and C. are charge and field maps of different plasmon modes, respectively.

Fig. 3.19 shows BEM simulated EEL spectra from the corner, edge and center of a 50 nm Au nanocube standing in vacuum. As seen in these EEL spectra, main plasmon resonances at the corner, edge and center are located at 2.33 eV, 2.38 eV and 2.50 eV, respectively. In Fig. 3.19B, charge maps of these plasmon modes are shown revealing that these are corner, edge and bulk modes of the nanocube, which were in fact respectively excited by a corner, edge and center beam. Their plasmon maps, presented in Fig. 3.19C, show the distribution of these plasmon fields. As discussed earlier for the

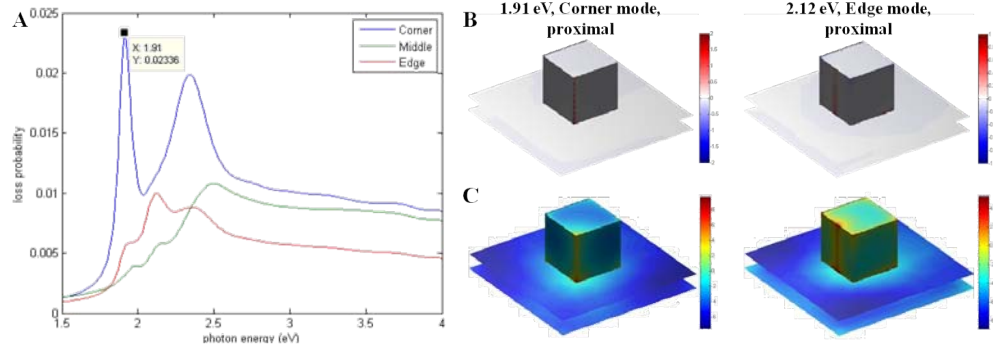


FIGURE 3.20: A. BEM simulated local EEL spectra of a 50 nm Au nanocube standing on a 15 nm thick Si_3N_4 substrate. Charge (B) and field (C) maps of two proximal modes arised due to interaction with the substrate.

Ag nanocubes, the presence of a substrate affects the plasmon resonances of the nanostructures. In Fig. 3.20A, we show BEM simulated local EEL spectra of a 50 nm Au nanocube standing on a 15 nm thick Si_3N_4 substrate. By comparing Fig. 3.19A and Fig. 3.20A one can see the shift of the plasmon resonances to lower energies and the presence of additional peaks due to the interaction with the substrate. In the Fig. 3.20B and Fig. 3.20C, we only show the charge and field maps of the proximal corner and edge modes that are generated due to the substrate effects, as the other distal modes are the same as the ones presented in Fig. 3.19. These proximal corner and edge modes are located at significantly lower energies of 1.91 eV and 2.12 eV, respectively, whose corresponding distal modes are located at 2.33 eV and 2.38 eV as shown in Fig. 3.19.

One can notice that the Au nanocube has more or less similar plasmon resonances to the Ag nanocubes at energies lower than 2.5 eV. The discrepancy at higher energies is due to the fact that Au plasmons suffer large "damping" at higher energies. Fig. 3.21A shows the dielectric function of Ag (in black) and Au (in blue), where the solid lines are for the real parts of the dielectric function and the dashed lines are for the imaginary parts. As seen in this figure, imaginary parts of the dielectric functions of Ag and Au are almost the same below ~ 1.9 eV resulting similar plasmonic behavior at the lower energy ranges. Fig. 3.21B shows the DDA simulated EEL spectra of bulk (volume) plasmon resonances for Ag and Au, where it is clear that the bulk plasmon mode of Au is located at 2.5 eV and the bulk plasmon mode of Ag is located at 3.8 eV. These simulated spectra are similar to the BEM simulated local EEL spectra obtained from the centers of the Ag nanocube (Fig. 3.10) and Au nanocube (Fig. 3.19). It should be noted here that comparing LSPR properties of Ag and Au nanostructures is not straight forward due to the fact that Ag nanoparticles have more intense and sharp LSPRs than Au nanoparticles [64]. In Ag nanoparticles, the overlapping of LSPRs and interband transitions is fairly small [53, 64], whereas the onset of interband transitions partially overlaps with the LSPRs of Au nanoparticles causing a decrease in LSPR intensity [64].

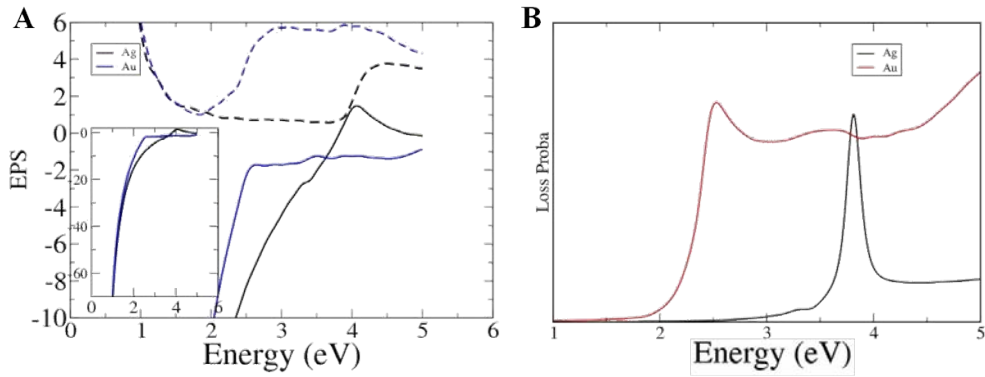


FIGURE 3.21: A. Dielectric function of Ag and Au, where the solid lines are for the real parts of the dielectric function and the dashed lines are for the imaginary parts. B. DDA simulated EEL spectra of bulk plasmon resonances of Ag and Au structures.

After showing BEM simulated plasmon resonances of Au nanocubes, we proceed with the Ag@Au core-shell nanocube simulations. Fig. 3.22A shows BEM simulated local EEL spectra from the corner, edge and center of a 50 nm Ag@Au core-shell nanocube with a rather thin shell of 1.5 nm Au. As seen in these figure, there are different plasmon peaks between ~ 2 eV and 3.8 eV, where the local EEL spectra from the corner and edge reveal the presence of quite wide peaks covering all the energy range. It should be noted here that experimental broadening is taken into consideration for these BEM simulated EEL spectra and such EEL spectra are quite similar to the experimentally observed EEL spectra shown in Fig. 3.14B. Plasmon maps of different proximal and distal modes are shown in Fig. 3.22B. One can understand these modes by comparing them with the plasmon resonances of pure Ag (Fig. 3.13) and Au (Fig. 3.19) nanocubes presented above. It seems the plasmon modes related to the Ag nanocube and the Au shell merge together and create conjunct, independent modes that are not the same as the ones for pure Ag or Au nanocubes. For instance, the lowest proximal corner mode for the Ag nanocube is located at 2.27 eV and it is located at 1.91 eV for the Au nanocube, whereas a proximal corner mode at 1.98 eV is observed for the case of Ag@Au core-shell nanocube. Likewise, other corner, edge and corner/edge modes have different energies than those observed for the pure Ag nanocube, whereas the resonances from the face plasmon mode of Ag located at 3.70 eV are present in the Ag@Au core-shell nanocube.

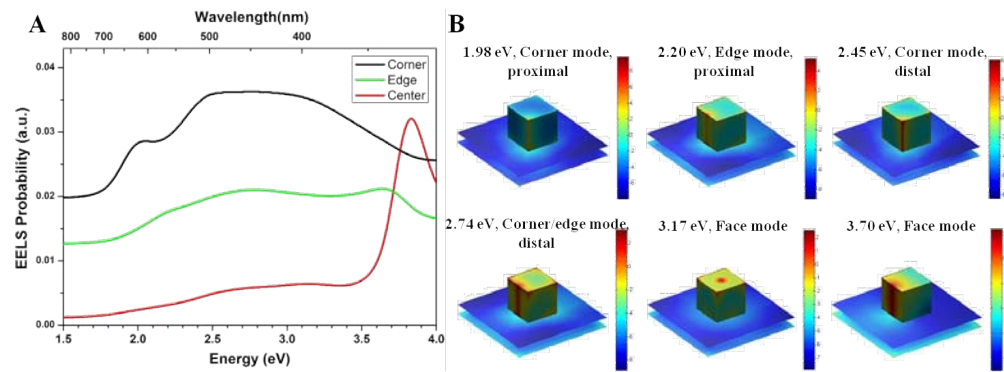


FIGURE 3.22: A. BEM simulated EEL spectra from the corner, edge and center of a 50 nm Ag@Au core-shell nanocube with a 1.5 nm shell thickness. B. Simulated plasmon maps of different proximal and distal modes.

3.4 Pinholed AuAg nanobox

3.4.1 Local plasmonic properties

Fig. 3.23A shows HAADF STEM micrograph of a 51 nm pinholed AuAg nanobox with a rectangular inner hole of 12 nm x 17 nm. In Fig. 3.23B selected area EEL spectra of the pinholed nanobox obtained from the upper left (in black) and lower right (in green) corners, upper edge (in blue), center hole (in orange) and bulk (in red) are shown. The EEL spectra obtained from the upper left and lower right corners and the upper edge reveal the presence of wide peaks, which may contain several LSPR modes, with the peak positions (the position of the maximum intensity) of ~ 2.9 eV, ~ 2.3 eV and ~ 2.7 eV, respectively. The EEL spectrum taken from the center hole of the pinholed AuAg nanobox shows the presence of a peak ~ 3.6 eV, which might be related to the surface plasmon mode of Ag. Moreover, a peak corresponding to the bulk plasmon resonance of Ag is observed for the EEL spectrum obtained from the bulk (in red, lower left part nanobox) of the nanobox.

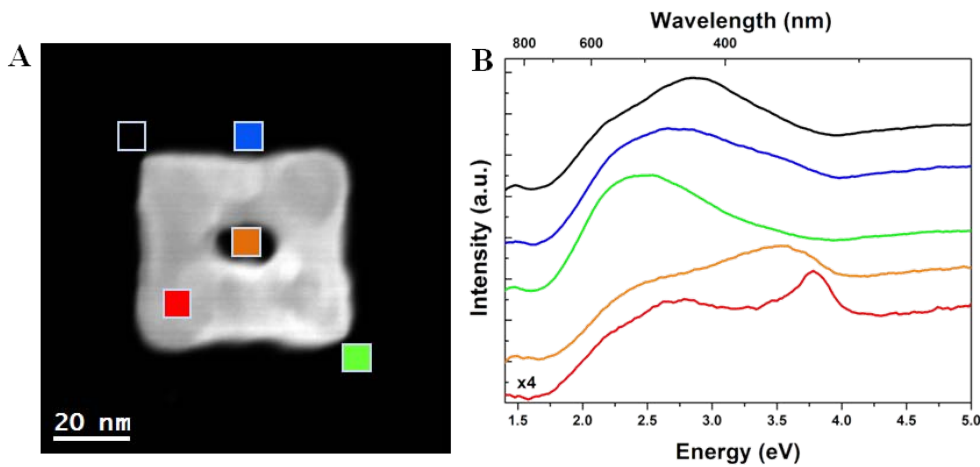


FIGURE 3.23: A. HAADF STEM micrograph of a 51 nm pinholed AuAg nanobox. B. Selected area EEL spectra of the upper left and lower right corners, upper edge, center hole and bulk of the pinholed nanobox (areas are indicated in HAADF STEM micrograph, which are 5 pixel by 5 pixel).

3.4.2 Processing of plasmonic properties

Fig. 3.24 shows the plasmon energy (A) and intensity (B) maps of the pinholed AuAg nanobox obtained by fitting a Gaussian between the energy ranges of 2.1 - 2.5 eV, 2.4 - 3.2 eV, 3.2 - 4.0 eV and 3.5 - 3.9 eV. The plasmon energy maps are obtained by fitting a Gaussian between the energy ranges of 2.1 - 2.5 eV and 2.4 - 3.2 eV seem to be distributed throughout the nanobox and surroundings with higher energies over the

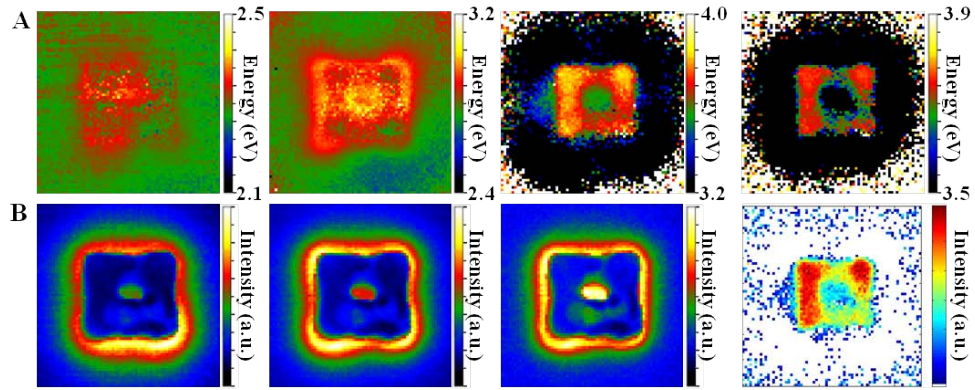


FIGURE 3.24: A. Plasmon energy maps of the pinholed AuAg nanobox, obtained by fitting a Gaussian between the energy ranges of 2.1 - 2.5 eV, 2.4 - 3.2 eV, 3.2 - 4.0 eV and 3.5 - 3.9 eV and B. their corresponding plasmon intensity maps. White pixels in the energy maps are out of fitting parameters. Notice that the plasmon intensity map between 3.5 and 3.9 eV has a different color code, where white pixels are the pixels with lowest intensity

nanobox, where the former is intense at the lower right corner and the latter is intense all around the nanobox including the inner hole. A wide Gaussian fitting is performed between 3.2 and 4.0 eV in order to reveal the distribution of surface plasmon resonances from the inner hole (peak located at ~ 3.6 eV) along with the plasmon resonance of the bulk mode of Ag. Additionally, a plasmon energy map just showing the bulk plasmon resonance of Ag between the energy values of 3.5 and 3.9 eV is presented in this figure, which reveals that even though the galvanic replacement is advanced enough to create voids, there is still pure Ag present in the pinholed AuAg nanobox and it is located through the left edge and upper right corner. As given in Fig. 3.23B, the plasmon peak obtained from the lower right corner of the pinholed AuAg nanobox has lower energy than that of the upper left corner, which can now be explained with the local structural differences as evidenced in Fig. 3.24 by mapping the bulk plasmon resonance of Ag. Corresponding plasmon intensity maps of these energy maps are presented in Fig. 3.24B, revealing similar a behavior as those obtained for the Ag@Au core-shell nanocube except the presence of plasmon resonance inside the nanobox. Similarly, the plasmon intensity map for the bulk plasmon resonance of Ag is obtained by using MatlabTM.

Fig. 3.25 shows the BSS analysis of the EELS-SI obtained from the pinholed AuAg nanobox, showing the spectra of 5 components and their corresponding abundance maps. The component I shows a plasmon peak at ~ 2.3 eV, which is mostly due to the plasmon resonances of the lower right corner along with weak excitations from the upper edge. The component II shows the presence of a wide peak at 2.8 eV due to the plasmon resonances from the corners and, partially, edges of the nanobox. Another corner LSPR mode is shown in the component III at ~ 3.1 eV that is intense at the corners except lower right corner. The component IV located at ~ 3.5 eV shows high intensity excitations from

the inner hole and face of the nanobox. The bulk plasmon resonance of Ag is presented in the component V, with some outer contributions (see the relevant abundance map) due to the wide peak of the component.

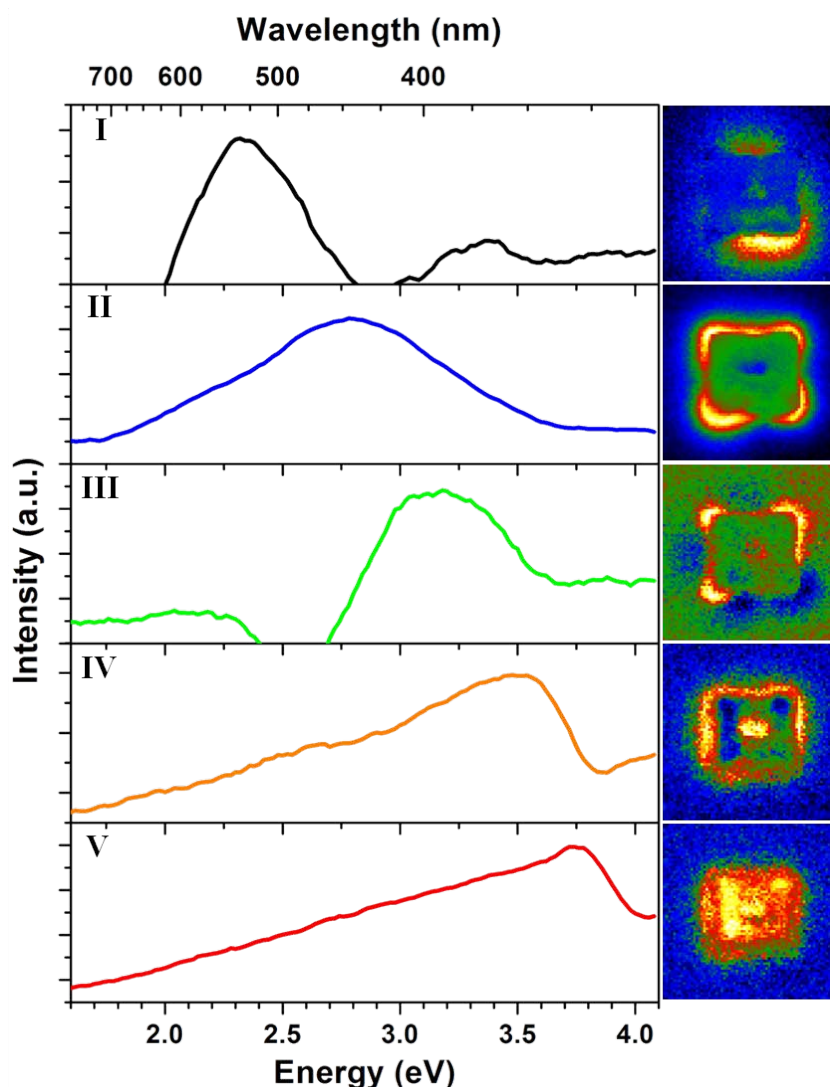


FIGURE 3.25: BSS analysis of the pinholed AuAg nanobox: Spectra of the 5 components and their corresponding abundance maps.

Fig. 3.26 shows the VCA analysis of the EELS-SI obtained from the pinholed AuAg nanobox, revealing the spectra of 5 composites and their corresponding abundance maps. The component I shows the presence of a peak at ~ 2 eV with two other smaller peaks at higher energies, however, its corresponding abundance map suggests that these peaks are due to the background contribution. Component II shows a plasmon peak at ~ 2.3 eV which is due to the excitations from the lower right corner, with some contributions from the lower edge. Another plasmon mode at ~ 2.6 eV is shown in the component III, which is mainly due to the excitations from the lower corners and upper edge with contributions from the other corners and edges. The component IV is also shows a

corner/edge mode at ~ 3 eV, where no plasmon resonance from the lower right corner is observed for this component. The bulk plasmon mode of the Ag is presented in component V where we have adjusted the contrast of the abundance map in order to give a better presentation about the intensity distribution within the nanobox, which reveals the presence of Ag along the left edge and upper right corner (quite similar to the maps presented in Fig. 3.24).

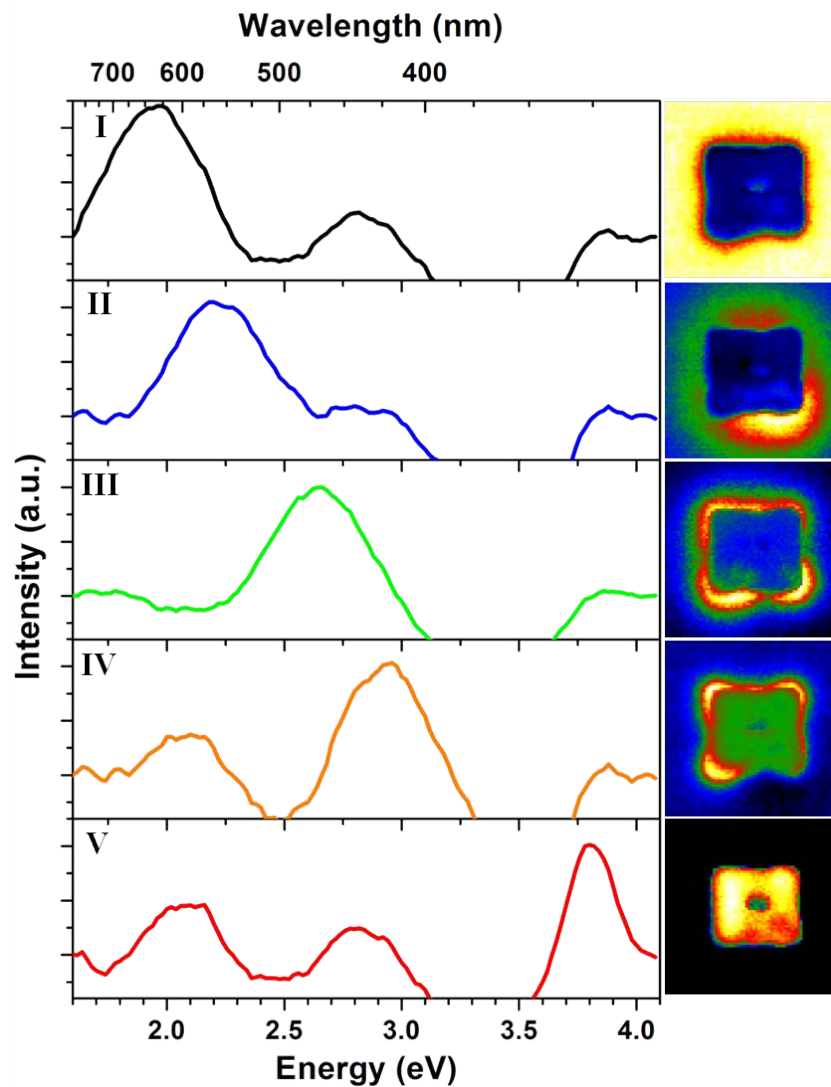


FIGURE 3.26: VCA analysis of the pinholed AuAg nanobox: Spectra of the 5 components and their corresponding abundance maps.

Table 3.3 shows the energy values of different components obtained by Gaussian fitting, BSS and VCA routines. It should be noted here that the energy values of the components for the Gaussian fitting are given as ranges of energies, which indicated the range of peak fitting. Energy values of the dominant peaks in the 5 different components obtained by BSS and 4 different components obtained by VCA are listed in this table. As its

abundance map revealed no specific features, component I of the VCA in Fig. 3.26 is shown here.

TABLE 3.3: Comparison of the plasmon components obtained by Gaussian fitting, BSS and VCA routines for the pinholed AuAg nanobox.

	Gaussian fitting	BSS	VCA
1st component	2.1-2.5 eV	~2.3 eV	~2.3 eV
2nd component	2.4-3.2 eV	2.8 eV	~2.6 eV
3rd component	3.2-4.0 eV	~3.1 eV	~3.0 eV
4th component	3.5-3.9 eV	~3.5 eV	~3.8 eV
5th component		~3.75 eV	

3.4.3 Boundary element method (BEM) simulations

When we compare the plasmonic properties of the Ag@Au core-shell nanocube and pinholed AuAg nanobox, we see that both nanostructures contain Ag-related plasmon resonances and the energies of some particular plasmon modes such as corner modes are more or less similar for both nanostructures, whereas, naturally, their distributions are different due to the presence of voids in the pinholed nanobox.

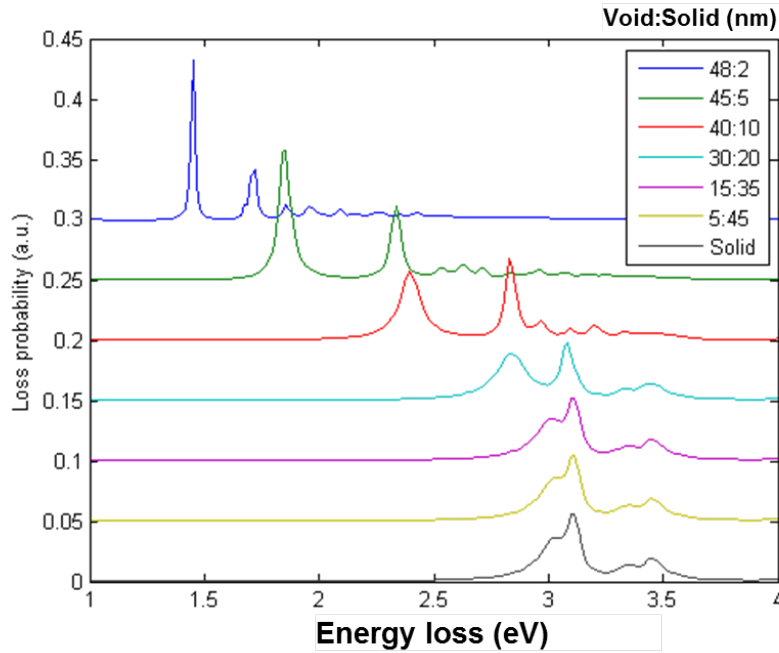


FIGURE 3.27: BEM simulated EEL spectra revealing the effect of void size for Ag nanostructures from 50 nm Ag nanocubes to 50 nm Ag nanobox with 2 nm thick walls.

In order to better understand the effect of voids and to be able to distinguish them, if possible, from the compositional effects, we have simulated 50 nm Ag nanoboxes with various wall thicknesses (Fig. 3.27). As seen in these BEM simulated EEL spectra, plasmon peaks of the 50 nm Ag nanocube shift to lower energies as the void size increases, in compliance with the above presented plasmon hybridization mechanism [63]. It is also worth noting that their intensities, i.e. loss probabilities, increase along with the increasing void size. These simulation results clearly suggest the powerful effect of morphological changes in the plasmonic properties of Ag nanostructures. It should be reminded that compositional changes in the AuAg nanostructures lead to morphological changes to some extent in accordance with the galvanic replacement reaction (Fig. 3.1). Therefore, it is safe to say that morphological changes have more dominant effects of the plasmonic properties of AuAg nanostructures synthesized via galvanic replacement reaction.

3.5 Single-walled AuAg nanobox

3.5.1 Local plasmonic properties

Fig. 3.28A shows HAADF STEM micrograph of a 50 nm single-walled AuAg nanobox with a wall thickness of ~ 7 nm. In Fig. 3.28B selected area EEL spectra of the single-walled nanobox obtained from the upper left (in black) and lower right (in green) corners, upper edge (in blue) and center (in red) are shown. As seen in this figure, the energy of plasmon peak is quite similar for the surroundings of the nanobox, i.e. upper left and lower right corners, upper edge, which is at 2.1 eV, however, the shape of the peaks differ from location to location where the presence of a shoulder peak at ~ 2.3 eV for the upper left corner can be observed. It should be noted here that the plasmon peak shifts to higher energies at the center of the nanobox, where the presence of two peaks located at ~ 2.2 eV and ~ 2.5 eV is evident in Fig. 3.28B.

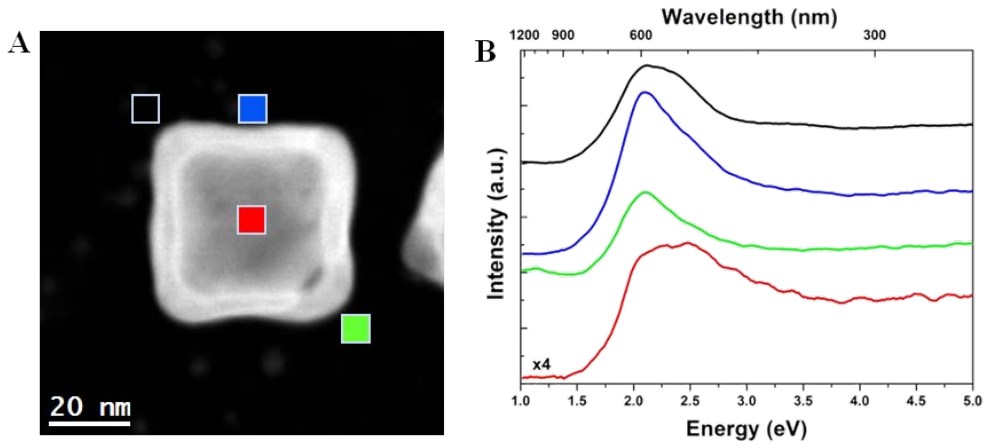


FIGURE 3.28: A. HAADF STEM micrograph of a 50 nm single-walled AuAg nanobox with ~ 7 nm wall thickness. B. Selected area EEL spectra of the upper left and lower right corners, upper edge, center of the nanobox (areas are indicated in HAADF STEM micrograph, which are 5 pixel by 5 pixel).

3.5.2 Processing of plasmonic properties

Since only one dominant peak is observed in Fig. 3.28B, we have obtained a plasmon energy map by fitting a Gaussian between the energy range between 1.9 and 2.4 eV for the single-walled AuAg nanobox as shown in Fig. 3.29A, which shows an enhanced energy field at the upper left corner and at the center of the nanobox. Fig. 3.29B corresponds to the plasmon intensity maps showing the distribution of the plasmons around the nanobox almost homogeneously.

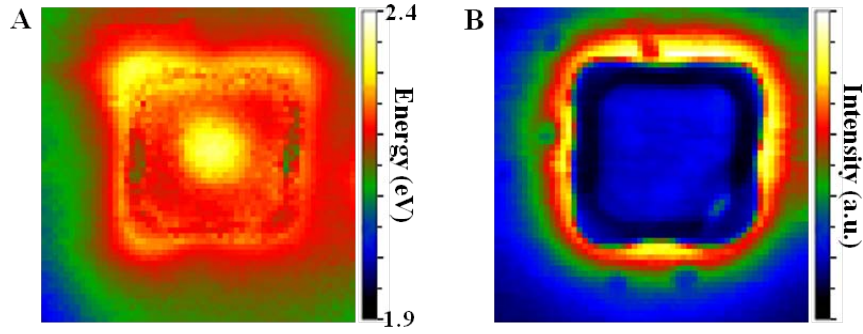


FIGURE 3.29: A. Plasmon energy map of the single-walled AuAg nanobox, obtained by fitting a Gaussian between the energy range between 1.9 and 2.4 eV and B. its corresponding plasmon intensity map.

Fig. 3.30 shows the BSS analysis of the EELS-SI obtained from the single-walled AuAg nanobox, showing the spectra of 3 components and their corresponding abundance maps. Although, we could fit only 1 Gaussian to the EELS data of the single-walled AuAg nanobox, it was possible to decompose the data to 3 components excluding the background. The component I shows a peak at ~ 1.9 eV, which is mostly due to the excitation from the left edge/face. The component II shows a plasmon resonance peak located at ~ 2.1 eV, whose abundance map reveals that this LSPR mode is present at the upper, right and lower edges/faces with some contributions from the corners (except for the upper left corner). A wide peak located at ~ 2.4 eV is shown for the component III, which is present almost all around the nanobox as well as the inner hole with weaker intensities.

Fig. 3.31 shows the VCA analysis of the EELS-SI obtained from the single-walled AuAg nanobox, showing the spectra of 3 components and their corresponding abundance maps. First component in this figure shows a plasmon peak located at ~ 2 eV with an additional peak at ~ 2.6 eV whose abundance map reveals that this LSPR mode is present all around the nanobox except the upper left corner. The component II reveals the presence of a plasmon peak at ~ 2.2 eV which correspond to the plasmon excitations from the edges/faces of the nanobox with contributions from the corners. A third component shows a plasmon peak at ~ 2.5 eV with a shoulder at ~ 2.3 eV and an additional peak at 2.06 eV and its corresponding abundance map reveals that this mode (more accurately, these peaks) is due to the resonances from the "bulk" of the nanobox in addition to the upper left corner and center of the nanobox.

It should be noted here that the plasmon resonances of the single-walled AuAg nanobox has several differences compared to the above presented nanostructures (namely, Ag nanocube, Ag@Au core-shell nanocube and pinholed AuAg nanobox) due to structural effects. First of them is the distributions of elements more homogeneously compared

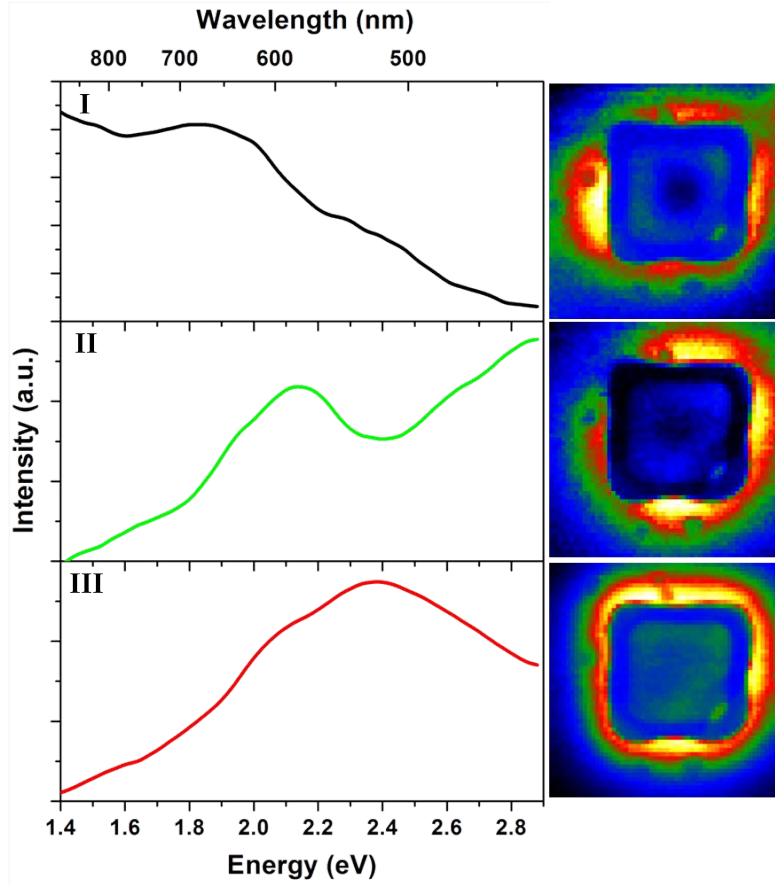


FIGURE 3.30: BSS analysis of the single-walled AuAg nanobox: Spectra of the 3 components and their corresponding abundance maps.

to the other structures [69], which leads to the existence of plasmon modes that are not dependent on local chemical differences. Secondly, presence of a inner void results in more homogeneous distribution of plasmon resonances around the nanoboxes [140], which are also evident from the above presented experimental results.

3.5.3 Boundary element method (BEM) simulations

In the following, we present the BEM simulation studies conducted on the single-walled AuAg nanobox. We have simulated a 50 nm nanobox with 7 nm thick walls, which is the size of the experimentally investigated nanobox (Fig. 3.28). During the STEM-EDX studies, we have found that single-walled AuAg nanoboxes are composed of 62 ± 7 at.% Au and 38 ± 7 at.% Ag. Due to the large standard deviations of about 7 at.%, we have simulated the single-walled AuAg nanobox with a composition of 60 at.% Au and 40 at.% Ag, assuming that Au and Ag are homogeneously distributed throughout the nanobox. Since we have already discussed the effects of substrate extensively, we directly simulate the single-walled AuAg nanobox by considering the effects of 15 nm thick Si_3N_4 substrate. Fig. 3.32 shows the BEM simulated EEL spectra from the corner,

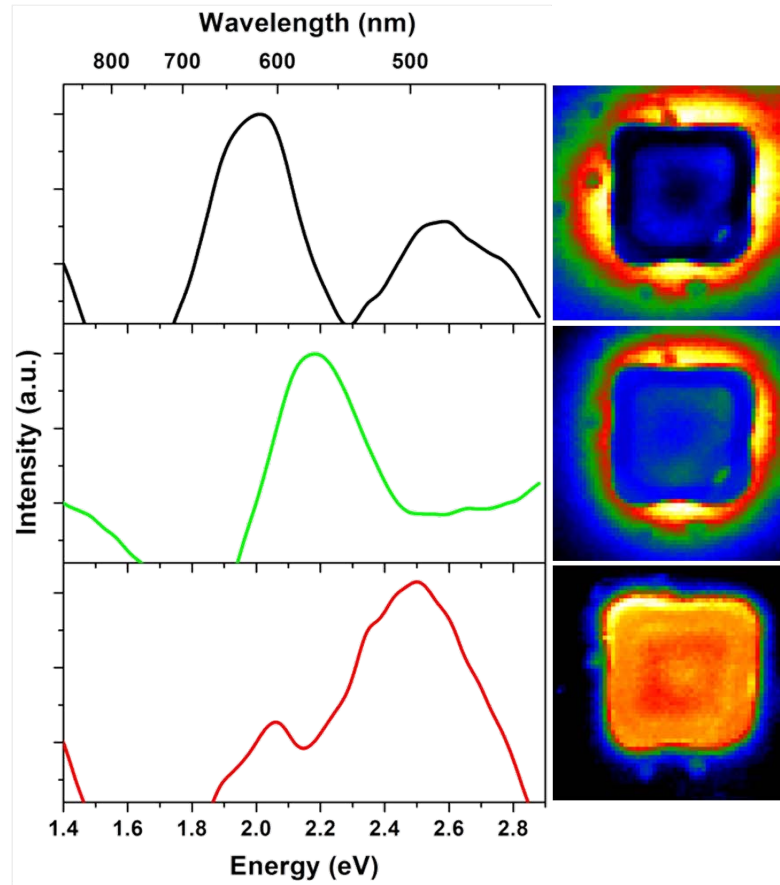


FIGURE 3.31: VCA analysis of the single-walled AuAg nanobox: Spectra of the 3 components and their corresponding abundance maps.

edge and center of the nanobox along with the structural model used for simulations and the sketch of the nanobox. As it can be seen from the structural model, these simulations are conducted for a nanobox with sharp corners. Simulated EEL spectra are quite similar to those obtained experimentally (Fig. 3.28) with $\pm \sim 0.1$ eV differences revealing accuracy of the assumptions about shape and composition. However, it should be noted here that the local differences in the morphology (for instance lower right corner being rounded, see Fig. 3.28A) would affect the distribution of plasmon resonances, since these EEL spectra are obtained from selected areas of a corner, an edge and the center of the nanobox, similar to the EEL spectra presented in (Fig. 3.28B). One needs 3-D analysis in order to take every morphological change into account, however it is safe to say that our simulations fit well with the experimental results.

Fig. 3.33 shows BEM simulated plasmon maps of the single-walled AuAg nanobox with sharp corners. 4 different maps are obtained at 1.94 eV, 2.16 eV, 2.44 eV and 2.62 eV on the basis of the peaks at Fig. 3.32. As seen in these maps, the plasmon resonance located at 1.94 eV are confined in the corners with some small contributions from the edges. However, such a well-defined corner mode could not be obtained experimentally (with

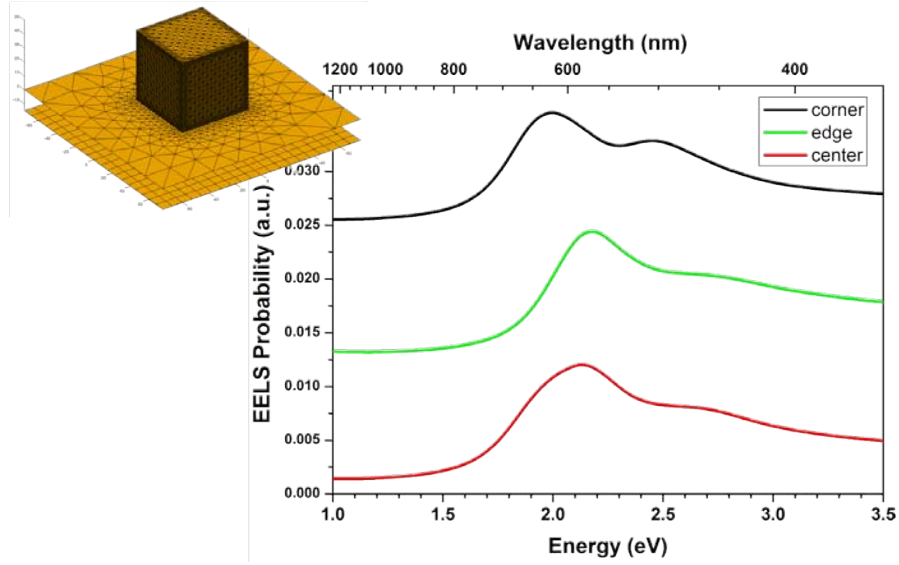


FIGURE 3.32: BEM simulations of a 50 nm single-walled AuAg nanobox with sharp corners: Model for the simulations and simulated EEL spectra from the corner, edge and center of the nanobox.

all three processing methods) probably due to the fact that experimentally investigated nanobox does not have sharp corners. The main plasmon mode located at around 2.16 eV for the edges and center of the nanobox and its plasmon map reveals that this mode is distributed homogeneously around the nanobox. This simulated plasmon map fits well with the experimentally observed maps shown in Fig. 3.29, Fig. 3.30 and Fig. 3.31 and with the literature suggesting that the plasmon modes of hollow nanostructures would be distributed homogeneously due to the coupling of the inner and outer plasmon resonances [61, 140]. The plasmon maps of two other modes located at 2.44 eV and 2.62 eV are also shown in this figure. We could not observe these relatively higher energy peaks clearly in the experimental EEL spectra (Fig. 3.28B) as they are shadowed by the tail of the background. Yet, we could see some similar contributions in the components III of BSS (Fig. 3.30) and VCA (Fig. 3.31) analyses.

Fig. 3.34 shows the BEM simulated plasmon maps of the single-walled AuAg nanobox where the same modes presented in Fig. 3.33 are shown in 3D with a corner beam excitation. As discussed previously in detail, presence of a substrate affects the plasmonic properties of the nanostructures. However, it is worth noting here that the distinctness of the proximal and distal modes is not as clear as a solid nanostructure (for instance, see Fig. 3.11 for the Ag nanocube) in the case of this hollow nanostructure. It may be due to the fact that the inner modes, which are not in contact with the plasmons, hence distal, are coupling with the outer modes and making hard to distinguish what is distal and what is proximal in hollow nanostructures.

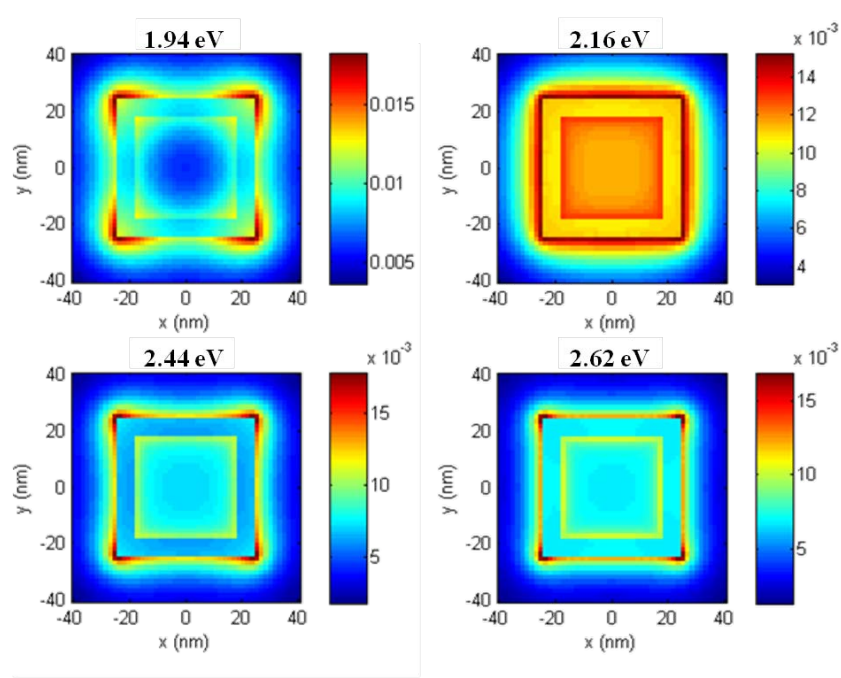


FIGURE 3.33: BEM simulations of field maps of 50 nm single-walled AuAg nanobox with sharp corners, obtained from the plasmon resonances at 1.94 eV, 2.16 eV, 2.44 eV and 2.62 eV.

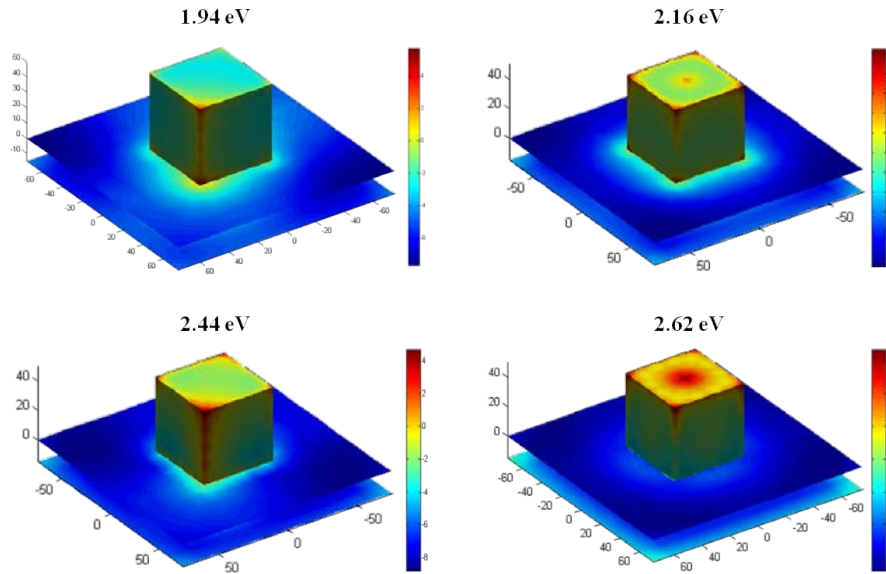


FIGURE 3.34: BEM simulations of 50 nm single-walled AuAg nanobox showing field maps of different plasmon modes in 3D.

Even though the above presented BEM simulations of the plasmon resonances of single-walled AuAg nanobox are in good agreement with the experimental data, we have simulated single-walled AuAg nanoboxes with smoother corners because of the inability to observe well-confined corner modes in the experimental results as suggested by the BEM simulations presented in Fig. 3.33. Fig. 3.35 shows the model of the nanobox

with smooth corners and simulated EEL spectra from the corner, edge and center of the nanobox. It is shown that plasmon peaks shifts to higher energies with the truncation of the corners where, for instance, the main peak from the corner is located at ~ 2.16 eV, which is located at ~ 1.94 eV for the nanobox with sharp corners (Fig. 3.32) and observed at ~ 2.1 eV experimentally (Fig. 3.28B). It is also visible from these simulated EEL spectra that the peaks at higher energies have lower intensities than those of the nanobox with sharp corners and mostly hidden by the tail of the main plasmon peaks.

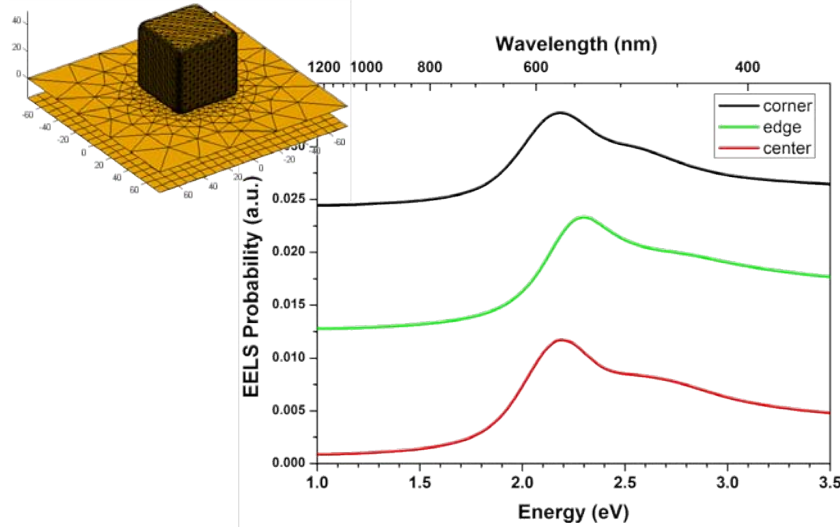


FIGURE 3.35: BEM simulations of a 50 nm single-walled AuAg nanobox with smooth corners: Model for the simulations and simulated EEL spectra from the corner, edge and center of the nanobox.

Fig. 3.36 shows the BEM simulated plasmon maps of a 50 nm single-walled AuAg nanobox with smooth corners for the resonances located at 2.16 eV, 2.28 eV, 2.50 eV and 2.74 eV. As the corners of the nanobox become smoother, corner and edge modes merge together and previously observed well-confined corner modes become a rather homogeneously distributed mode around the nanobox (mode at 2.16 eV). The plasmon resonance at 2.28 eV is also homogeneously distributed around the nanobox. These two modes seem to be equivalent of the components I and II of the VCA analysis shown in Fig. 3.31, where the experimentally observed maps may face some morphological inhomogeneities.

Table 3.4 shows the energy values of different components obtained by Gaussian fitting, BSS and VCA routines for the single-walled AuAg nanobox. Different from above presented tables summarizing the experimentally obtained results, we add the results obtained by BEM simulations to the comparison as we have tried to get the best fit with the experimental results for the single-walled AuAg nanoboxes. BEM results obtained on the single-walled AuAg nanobox with sharp corners are listed as BEM-1 and BEM results on the single-walled AuAg nanobox with smooth corners are listed as BEM-2.

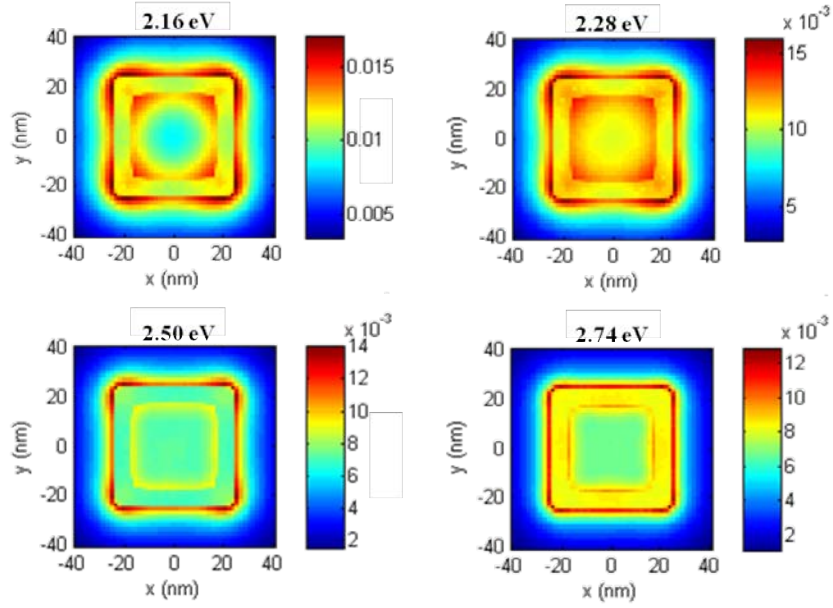


FIGURE 3.36: BEM simulations of a 50 nm single-walled AuAg nanobox with smooth corners: field maps of the plasmon resonances at 2.16 eV, 2.28 eV, 2.50 eV and 2.74 eV.

As presented above, only one component is obtained with Gaussian fitting between 1.9-2.4 eV. It is shown that components obtained by BSS have slightly lower energies than those obtained by VCA. A good agreement between the energy values of experimentally obtained components and BEM simulated components are shown in this table.

TABLE 3.4: Comparison of the plasmon components obtained by Gaussian fitting, BSS and VCA routines for the single-walled AuAg nanobox along with the BEM simulation results on the single-walled AuAg nanoboxes with sharp (BEM-1) and smooth (BEM-2) corners.

	Gaussian fitting	BSS	VCA	BEM-1	BEM-2
1st component	1.9-2.4 eV	~1.9 eV	~2.0 eV	1.94 eV	2.16 eV
2nd component		~2.1 eV	~2.2 eV	2.16 eV	2.28 eV
3rd component		~2.4 eV	~2.5 eV	2.44 eV	2.5 eV
4th component				2.62 eV	2.74 eV

3.6 AuAg nanoframe

3.6.1 Local plasmonic properties

Fig. 3.37A shows HAADF STEM micrograph of a 48 nm AuAg nanoframe with a wall thickness of ~ 7 nm. In Fig. 3.37B selected area EEL spectra of the nanoframe obtained from the upper left corner (in black), upper (in blue) and lower (in green) edges and center (in red) are shown. Selected area EEL spectrum of the upper left corner shows the presence of a peak located at ~ 1.7 eV with a shoulder peak at ~ 1.9 eV, which is almost the same for the selected area EEL spectrum of the upper edge. The lower edge seems to contain plasmon resonances with two different energies of ~ 1.7 eV and ~ 2.1 eV. It should be noted here that the energy of the plasmon peak of obtained from the center void of the nanoframe shifts to a higher energy of ~ 2 eV, that is about 0.3 eV higher than that of the corners and edges. One can also notice that the main plasmon peak at ~ 2.1 eV for the single-walled AuAg nanobox shifted to ~ 1.7 eV for the AuAg nanoframe. Such a shift is related to the increased Au content causing the creation of more voids in the AuAg nanoframes [175, 293], resulting a shift to lower energies in compliance plasmon hybridization mechanism [63, 139, 294].

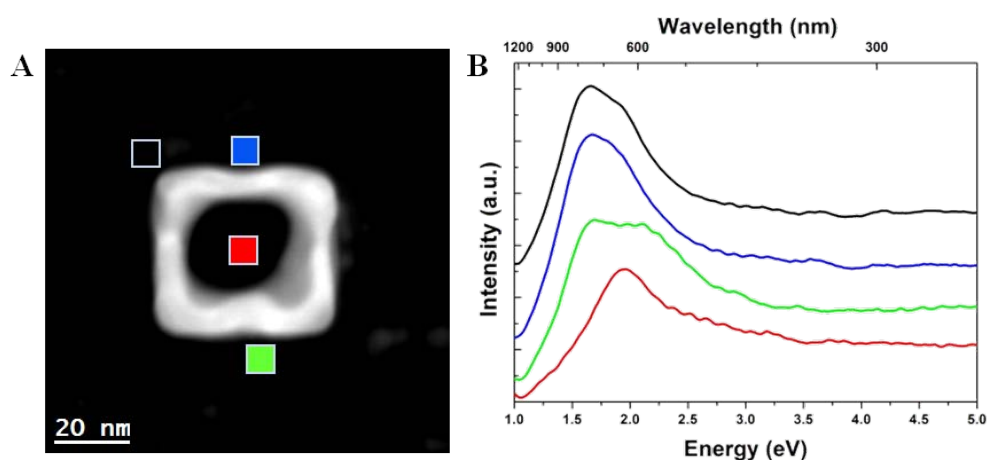


FIGURE 3.37: A. HAADF STEM micrograph of a 48 nm AuAg nanoframe with ~ 7 nm wall thickness. B. Selected area EEL spectra of the upper left corner, upper and lower edges and center of the nanoframe (areas are indicated in HAADF STEM micrograph, which are 5 pixel by 5 pixel).

3.6.2 Processing of plasmonic properties

In Fig. 3.38 a plasmon energy map and its corresponding plasmon intensity map obtained by fitting a Gaussian between the energy range between 1.6 and 2.1 eV in the EELS-SI of the AuAg nanoframe are shown. As seen in the plasmon energy map in Fig. 3.38A, the plasmon resonances of the nanoframe have an increased energy inside

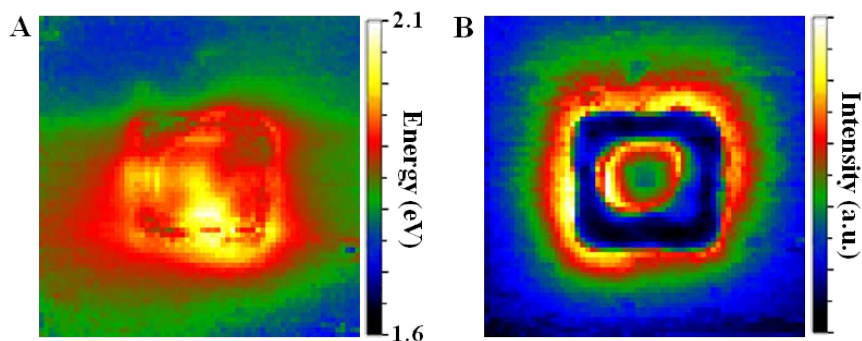


FIGURE 3.38: A. Plasmon energy map of the AuAg nanoframe, obtained by fitting a Gaussian between the energy range between 1.6 and 2.1 eV and B. its corresponding plasmon intensity map.

the nanoframe where the outer and inner part of the walls seem to interact over the course of this increased plasmon energy. Plasmon intensity map shown in Fig. 3.38B shows a somewhat homogeneous distribution of plasmon fields inside and outside of the nanoframe. An interaction between the inner and outer part over the left wall seems to be prominent in this plasmon intensity map.

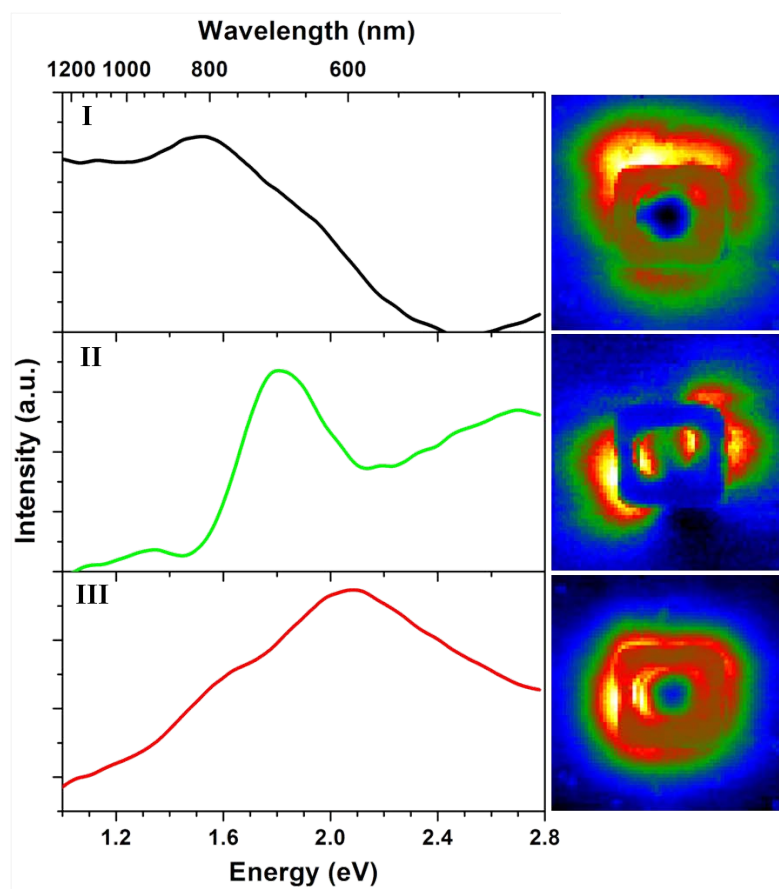


FIGURE 3.39: BSS analysis of the AuAg nanoframe: Spectra of the 3 components and their corresponding abundance maps.

Fig. 3.39 shows the BSS analysis of the EELS-SI obtained from the AuAg nanoframe, showing the spectra of 3 components and their corresponding abundance maps. First component in this figure shows a plasmon peak located at ~ 1.5 eV that is present along the upper edge of the nanobox with some additional resonances from the inner part and the lower edge of the nanoframe. The component II reveals the presence of a plasmon peak at ~ 1.8 eV which correspond to the plasmon excitations from the left edge and upper right corner (with some contributions from the edge) of the nanoframe that are present both inside and outside of the nanoframe. Such kind of interactions among the inner and outer plasmon resonances in hollow nanostructures were reported to yield enhanced sensitivity for the case of hollow nanostructures when compared to their solid counterparts [67, 140, 141]. The plasmon maps presented here are the first experimental evidence of such interaction of plasmon fields in hollow AuAg nanocage/nanoframe structures at the nanoscale. A third component shows a plasmon peak at ~ 2.1 eV with a shoulder at ~ 1.6 eV and its corresponding abundance map reveals that this mode is due to the resonances from the "bulk" and surroundings of the nanoframe along with a highly intense interaction between the inner and outer part of the left wall.

Fig. 3.40 shows the VCA analysis of the EELS-SI obtained from the AuAg nanoframe, showing the spectra of 3 components and their corresponding abundance maps, which are quite similar to the BSS analysis presented in Fig. 3.39 with slightly better separated components. Three components obtained by using VCA analysis are also located at ~ 1.5 eV, 1.8 eV and 2.1 eV, respectively, revealing quite similar abundance maps for the component I and III as the ones presented in Fig. 3.39 whereas the abundance map of the component II is more distributed around the nanoframe than that obtained by BSS.

3.6.3 Boundary element method (BEM) simulations

In the following, we present BEM simulations conducted on 48 nm AuAg nanoframe with 7 nm thick walls assuming that they are composed of 70 % Au and 30 % Ag being homogeneously distributed throughout the nanoframe.

In Fig. 3.41 shows the BEM simulated local EEL spectra from the corner, edge and center of a 48 nm AuAg nanoframe with 7 nm thick walls, along with its associated model used for simulations. In this figure, we simulate a perfect nanoframe with completely hollow faces and sharp corners and observe plasmon resonances at energies ~ 1 eV, which are significantly lower than those observed experimentally (Fig. 3.37B). We believe this is simply due to the shape effects where experimentally studied AuAg nanoframe has partially covered faces and rounded corners, which causes to shift of plasmon resonances

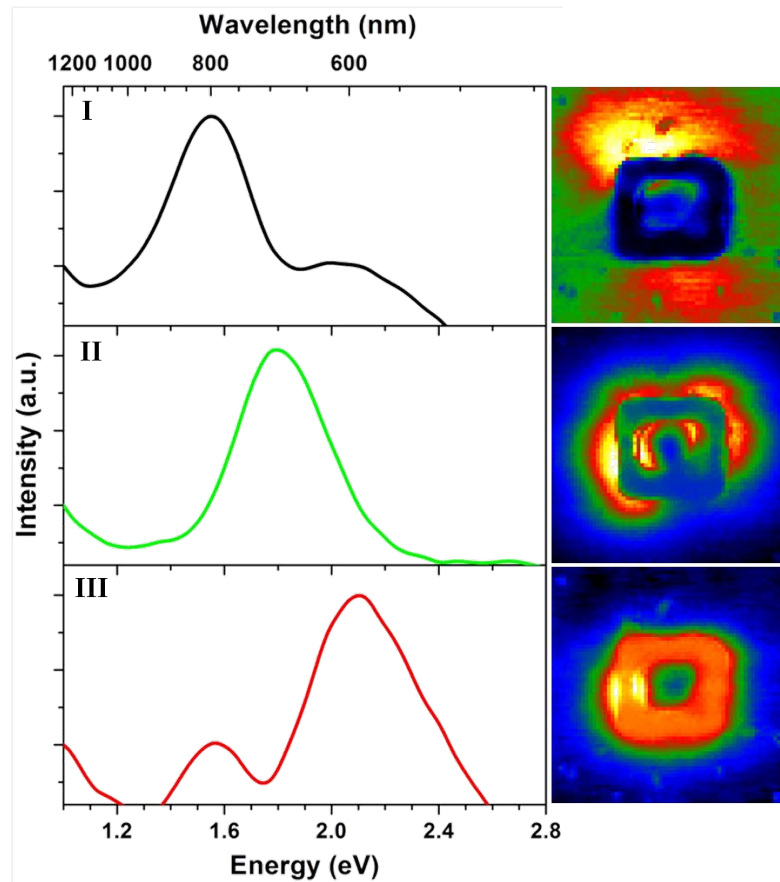


FIGURE 3.40: VCA analysis of the AuAg nanoframe: Spectra of the 3 components and their corresponding abundance maps.

to higher energies compared to the simulated perfect nanoframe case. Aside from its similarity with the experimental case, we can understand the plasmonic behavior of perfect AuAg nanoframes with these simulation results. The main plasmon resonance from the corners of the nanoframe is located at ~ 1 eV and two other peaks are observed at ~ 1.4 eV and ~ 1.8 eV. The main plasmon resonance of the edges is shifted to slightly higher energy of ~ 1.1 eV. It is important to note that the nanoframe contains relatively intense plasmon resonances at the center point with energies similar to those of corner and edge, even though the center point is in vacuum and at a distance of 17 nm from the walls.

Fig. 3.42 shows BEM simulated plasmon maps of the 48 nm AuAg nanoframe obtained from the plasmon resonances at 1.047 eV, 1.13 eV, 1.43 eV and 1.83 eV (Fig. 3.41). The mode at 1.047 eV seems to be highly intense at the corners, yet with some contributions from the edges. In other words, this corner mode is not confined to the corners but it is in interaction with the edges of the nanoframe. Another mode at 1.13 eV reveals quite similar distribution of plasmon resonances except the edges having more intense plasmon fields than the mode at 1.047 eV. These two modes are well distributed around

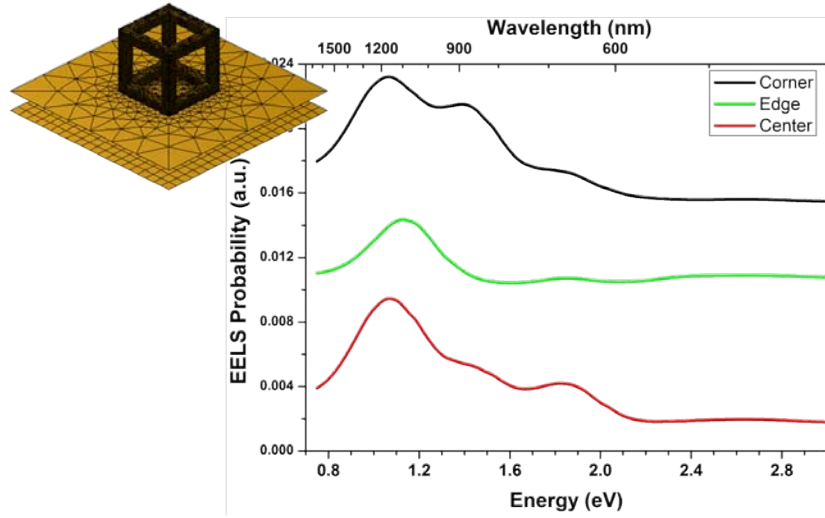


FIGURE 3.41: BEM simulated EEL spectra from the corner, edge and center of a 48 nm AuAg nanoframe as shown in the upper left model.

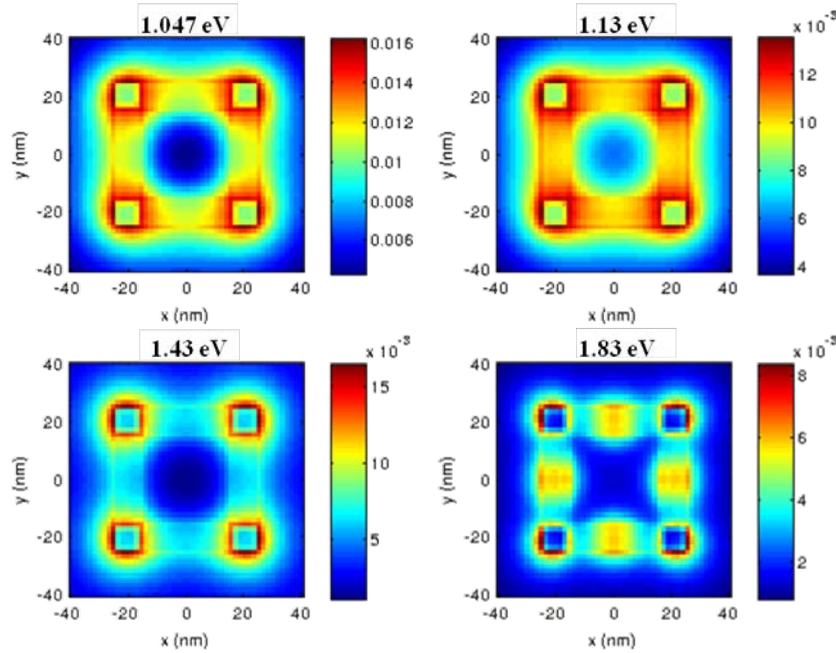


FIGURE 3.42: BEM simulations of a 48 nm AuAg nanoframe: field maps of the plasmon resonances at 1.047 eV, 1.13 eV, 1.43 eV and 1.83 eV.

the nanoframe yet somehow locally confined due to the perfect shape of the nanoframe. For instance, the mode at 1.43 eV seems to be present only at the corners, whereas the mode at 1.83 eV is present both at the corners and at the middle point of the edges. It should be stressed here that even if the two modes at 1.047 eV and 1.13 eV were present in the experimentally investigated nanostructure, it would be impossible to decompose them as two separate components given the energy resolutions of the EELS experiments being ~ 0.130 eV. Therefore, instead of these two separated maps with slight differences in plasmon field distributions, we would see a sum mode covering both of these modes.

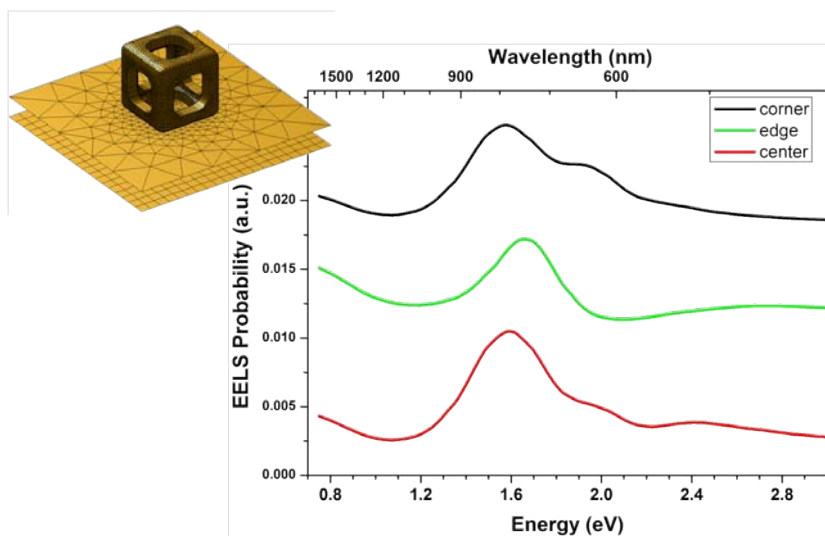


FIGURE 3.43: BEM simulated EEL spectra from the corner, edge and center of a 48 nm AuAg nanoframe which is more similar to the experimentally investigated nanoframe with its partially filled faces and rounded corners as shown in the upper left model.

After studying the case of perfect nanoframes, we have simulated another nanoframe that resembles the experimentally investigated one with its partially filled faces and smooth corners as shown in the model in Fig. 3.43. As seen in the local EEL spectra from the corner, edge and center of the AuAg nanoframe, plasmon resonances shift to higher energies as the faces get filled and corners being rounded. This simulation model, as the experimentally studied nanostructure in Fig. 3.37A, is kind of an intermediate nanostructure between the nanobox and nanoframe, yet, we refer it as a nanoframe in order to emphasize its differences with the nanobox. Although this structural model and its associated BEM simulations consider a somewhat homogeneously corroded nanoframe, which might not be the case for the experimental nanoframe, it has been seen that the main plasmon resonances for this "realistic" AuAg nanoframe are located at ~ 1.6 eV, which are quite similar to those observed experimentally (Fig. 3.37B).

Fig. 3.44 shows BEM simulated plasmon maps of the plasmon resonances at 1.558 eV, 1.685 eV, 1.94 eV, 2.237 eV, 2.407 eV and 2.748 eV in the AuAg nanoframe. Similar to the above presented perfect nanoframe case, the main corner and edge modes located at 1.558 eV, that is more confined around the corners, and at 1.685 eV, that is present all around the nanoframe, have quite similar energies and it would be impossible to distinguish them during the EELS experiments. Instead, one would observe plasmon fields distributed almost homogeneously around the nanoframe, similar to the one presented in Fig. 3.38B. Two other modes that are confined around the corners are located at 1.94 eV and 2.237 eV. Another mode at 2.407 eV, which is fairly visible in the simulated EEL spectrum of the center, reveals plasmon fields at the corners and the middle points

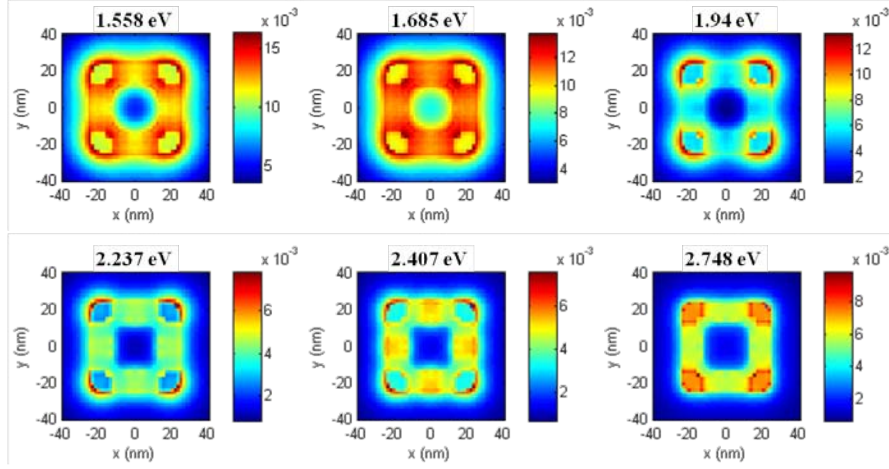


FIGURE 3.44: BEM simulations of a 48 nm AuAg nanoframe with partially filled faces and smooth corners: field maps of the plasmon resonances at 1.558 eV, 1.685 eV, 1.94 eV, 2.237 eV, 2.407 eV and 2.748 eV.

of the edges. The mode at 2.748 eV, which shows a bulk plasmon-like field distribution is barely visible in the EEL spectra as it gets hidden in the background.

Fig. 3.45 shows BEM simulated 3D field maps of the plasmon resonances located at 1.558 eV, 1.685 eV and 1.94 eV of the realistic AuAg nanoframe. A/B, C/D and E/F are the same modes yet, the maps in A, C and E are obtained by a corner beam excitation and the maps in B, D and F are obtained by an edge beam excitation. The contributions from almost all around the nanoframe are clearly visible especially in the maps obtained with an excitation beam placed at the edge, thus, homogeneously distributed plasmon fields such as the ones shown in Fig. 3.44 could be obtained.

Table 3.5 shows the energy values of different components obtained by Gaussian fitting, BSS and VCA routines for the AuAg nanoframe. Moreover, BEM simulation results on a perfect nanoframe with sharp corners and edges (Fig. 3.41) and a more realistic nanoframe with smooth corners and partially filled voids are listed as BEM-1 and BEM-2, respectively. As seen in this table, BSS and VCA processes generate components with the same energy values. Moreover, there is a good qualitative agreement with the experiments and BEM simulations on the realistic AuAg nanoframe (BEM-2), except for the higher energy components which are mostly hidden in the background of the experimental spectra.

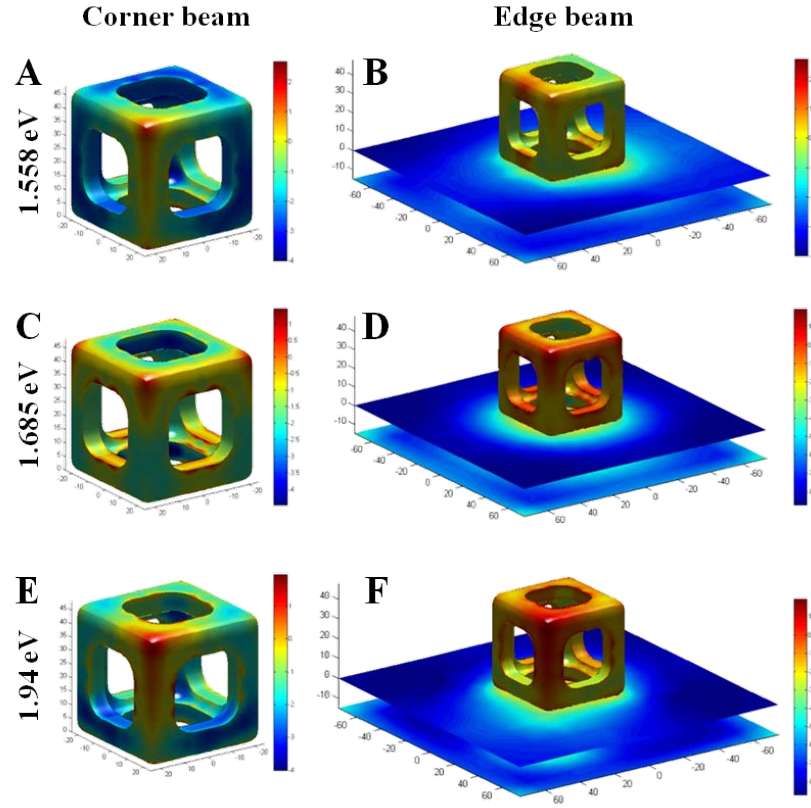


FIGURE 3.45: BEM simulated 3D field maps of the plasmon resonances located at 1.558 eV, 1.685 eV and 1.94 eV in the realistic AuAg nanoframe: A, C and E are plasmon fields excited by a corner beam and B, D and F are plasmon fields excited by an edge beam.

TABLE 3.5: Comparison of the plasmon components obtained by Gaussian fitting, BSS and VCA routines for the AuAg nanoframe along with the BEM simulation results on the perfect nanoframe with sharp corners and edges (BEM-1) and on a more realistic nanoframe with smooth corners and partially filled faces (BEM-2).

	Gaussian fitting	BSS	VCA	BEM-1	BEM-2
1st component	1.6-2.1 eV	~1.5 eV	~1.5 eV	1.047 eV	1.558 eV
2nd component		~1.8 eV	~1.8 eV	1.13 eV	1.685 eV
3rd component		~2.1 eV	~2.1 eV	1.43 eV	1.94 eV
4th component				1.83 eV	2.237 eV
5th component					2.407 eV
6th component					2.748 eV

3.7 Double-walled AuAg nanobox

3.7.1 Local plasmonic properties

Fig. 3.46A shows a HAADF STEM micrograph of a 50 nm AuAg double walled nanobox with an outer wall thickness of ~ 7 nm, where the inner box has an edge length of 26 nm with 5 nm thick walls. In Fig. 3.46B selected area EEL spectra of the double-walled nanobox obtained from the upper left corner (in black), upper edge (in green) and center (in red) are shown. The selected area EEL spectra obtained from the corner and upper edge reveals almost the same features with the main peak located at ~ 2 eV with a smaller peak at ~ 1.3 eV. It should be noted here that the peak at ~ 1.3 eV is present all over the spectrum image and generates plasmon map that is no different than the background. As seen in the selected area EEL spectrum obtained from the center of the double walled nanobox, the peak is shifted to ~ 2.2 eV that is 0.2 eV higher than those obtained for the surroundings of the nanobox.

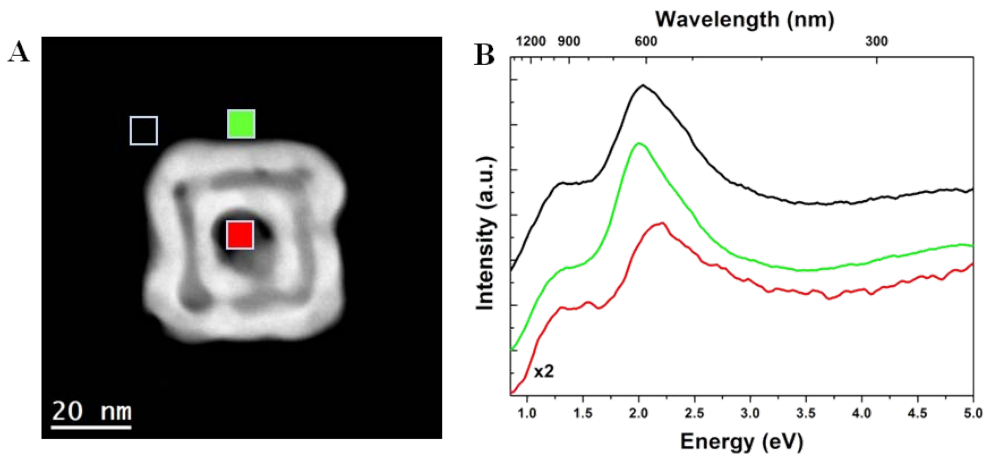


FIGURE 3.46: A. HAADF STEM micrograph of a 50 nm double-walled AuAg nanobox. B. Selected area EEL spectra of the upper left corner, upper edge and center of the double-walled nanobox (areas are indicated in HAADF STEM micrograph, which are 5 pixel by 5 pixel).

3.7.2 Processing of plasmonic properties

In Fig. 3.47 a plasmon energy map and its corresponding plasmon intensity map obtained by fitting a Gaussian between the energy range between 1.6 and 2.4 eV in the EELS-SI of the double-walled AuAg nanobox are shown. The plasmon energy map shows a homogeneous distribution of plasmon resonances at ~ 2.1 eV around the double-walled nanobox that is increased in the center of the nanobox and decreased among the walls. It is also interesting to see a systematical energy decrement with the increased distance from the nanobox, which is not common for the plasmon resonances and the

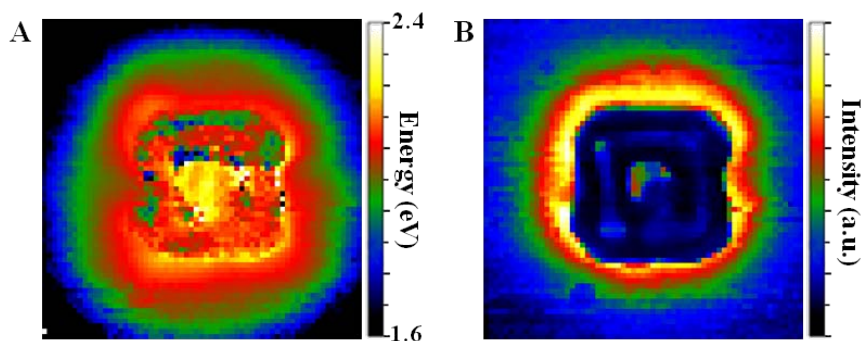


FIGURE 3.47: A. Plasmon energy map of the double-walled AuAg nanobox, obtained by fitting a Gaussian between the energy range between 1.6 and 2.4 eV and B. its corresponding plasmon intensity map.

reason for such a map is unknown. The plasmon intensity map presented in Fig. 3.47B shows almost perfectly homogeneous distribution of the plasmon resonances around the double-walled AuAg nanobox.

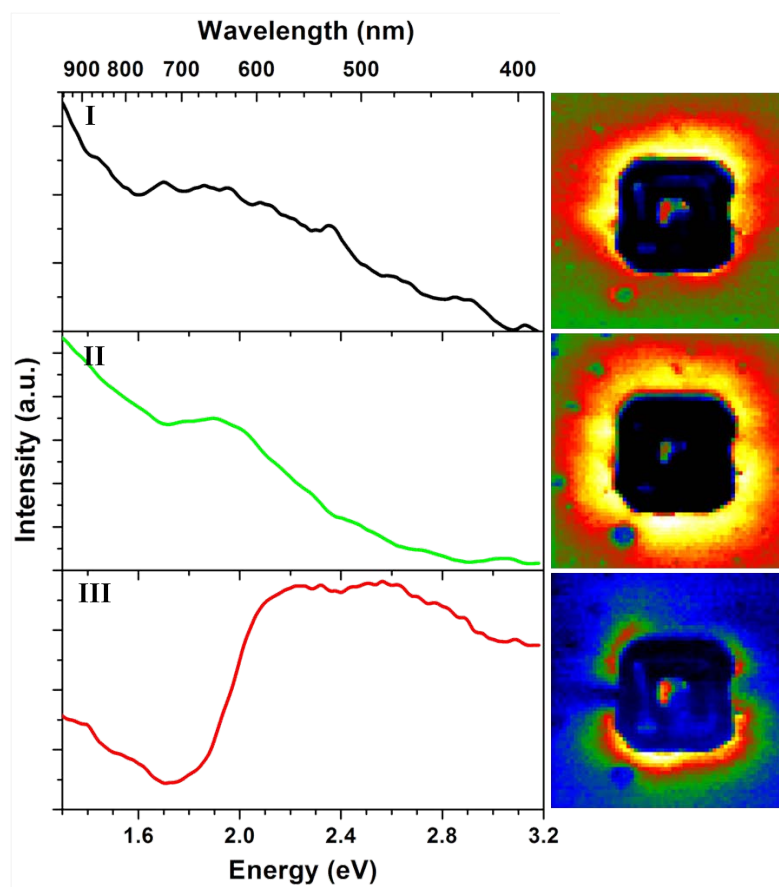


FIGURE 3.48: BSS analysis of the double-walled AuAg nanobox: Spectra of the 3 components and their corresponding abundance maps.

Fig. 3.48 shows the BSS analysis of the EELS-SI obtained from the double-walled AuAg nanobox, showing the spectra of 3 components and their corresponding abundance maps.

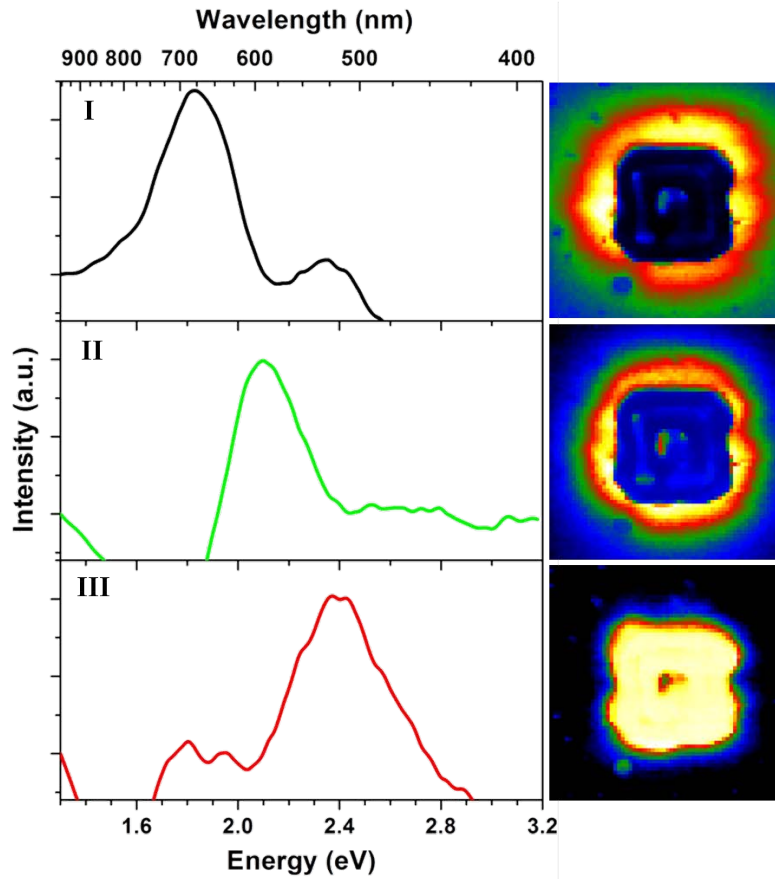


FIGURE 3.49: VCA analysis of the double-walled AuAg nanobox: Spectra of the 3 components and their corresponding abundance maps.

As seen in this figure, only the component II reveals a well separated plasmon peak located at ~ 1.9 eV and its corresponding abundance maps suggests that this LSPR mode is present all around the double-walled nanobox. Components I and III show some plasmon excitations from the upper and lower parts of the nanobox, respectively, however the fact that their spectra do not show any peak makes these abundance maps questionable. Therefore, BSS analysis on the double-walled AuAg nanobox was inconclusive.

Fig. 3.49 shows the VCA analysis of the EELS-SI obtained from the double-walled AuAg nanobox, showing the spectra of 3 components and their corresponding abundance maps. Unlike BSS analysis, VCA analysis on the double-walled AuAg nanobox generates 3 well separated components. Component I shows the presence of a plasmon peak at ~ 1.8 eV with a smaller peak at ~ 2.3 eV. Its corresponding abundance maps reveals that this mode is distributed around the nanobox with high intensities at the lower edge/face having lower intensity compared to the other parts. Component II shows a plasmon peak at ~ 2.1 eV which is due to the homogeneously distributed surface plasmon excitation around the double-walled nanobox. Component III shows a splitted plasmon peak at ~ 2.4 eV which corresponds to the plasmon excitations from the "bulk" of the

double-walled nanobox. As seen in this figure, in general, LSPR modes of the double-walled AuAg nanobox can be considered as homogeneously distributed throughout the nanobox.

Table 3.6 shows the energy values of different components obtained by Gaussian fitting, BSS and VCA routines for the double-walled AuAg nanobox. The only component obtained by Gaussian fitting is listed as an energy range between 1.6-2.4 eV, which is the range for the peak fitting. Only 1 of the 3 components obtained by BSS (Fig. 3.48) is listed in this table as it was hard to distinguish the energy values of other two components.

TABLE 3.6: Comparison of the plasmon components obtained by Gaussian fitting, BSS and VCA routines for the double-walled AuAg nanobox.

	Gaussian fitting	BSS	VCA
1st component	1.6-2.4 eV	~1.9 eV	~1.8 eV
2nd component			~2.1 eV
3rd component			~2.4 eV

3.8 Sensing with the hollow nanostructures

Localized surface plasmon resonances of the nanoparticles are known to be highly sensitive to the local environment, as well as to their size and shape, as it has been discussed in this chapter so far. Label-free optical sensing with plasmonic nanoparticles is based on the detection of adsorbate induced refractive index changes near or on the nanoparticles, which change the dielectric constant of the surrounding medium and can be measured by using UV-visible extinction spectroscopy [83, 84, 126, 133]. Adsorbate induced shifts in LSPR can be expressed as $\Delta\lambda_{max}$, which is simply given in the equation (3.1) [84]:

$$\Delta\lambda_{max} = \lambda_{max} < after > - \lambda_{max} < before > . \quad (3.1)$$

However, actual nanostructure plasmonic changes are too small for common absorption intensity (optical density) in biological and medical testing devices, especially if the sensing event is away from the nanoparticle surface. Therefore there is a need for increased sensitivity to unleash the power of plasmonic sensing, otherwise practical applications can be precluded. In this study, we detect the binding of antibodies to a protein corona [295] formed on single-walled AuAg nanoboxes and spherical Au nanoparticles for comparison. It is well known that when the nanoparticles are dispersed in physiological media, they are immediately coated by proteins, forming a protein corona that hardens with time [296] becoming a hard protein shell that provides the biological identity [297] of the nanoparticle, which is mainly composed by native Bovine Serum Albumin (BSA) [295]. Used as an antigen, this BSA is detected by BSA-Antibodies (Ab), as described in Fig. 3.50, where the first NP-protein interaction and the secondary protein-Ab interaction are detected and compared between spherical Au NPs and single walled AuAg nanoboxes. We use highly sensitive small 50 nm Au spherical NPs as a benchmark [298].

Fig. 3.50A shows the schematic representation of the primary (with BSA) and secondary (with anti-BSA) protein conjugation processes with spherical solid nanoparticles and hollow nanoboxes, where the coverage of nanostructures with BSA and further attachment of antibodies are illustrated. Fig. 3.50B shows the UV-visible spectra from the unconjugated spherical Au nanoparticles (left graph) and single-walled AuAg nanoboxes (right graph) in black. These spectra are used as reference and their response to the BSA conjugation are shown by red lines. Insets in both graphs are the close-up of the maximum intensity parts of the peaks. As can be seen in these UV-Vis spectra, the position of the LSPR peak of spherical Au nanoparticles do not change much whereas the shift in the LSPR peak of the AuAg nanoboxes is clearly visible. Similar differences between the Au nanoparticles and single-walled AuAg nanoboxes are also observed during the second conjugation event (shown in blue). Overall, it is clearly seen in Fig. 3.50C that about 5 times stronger shifts in the case of hollow AuAg nanoboxes are observed, especially in the second binding event, thanks to the enhancement of the localized EM field

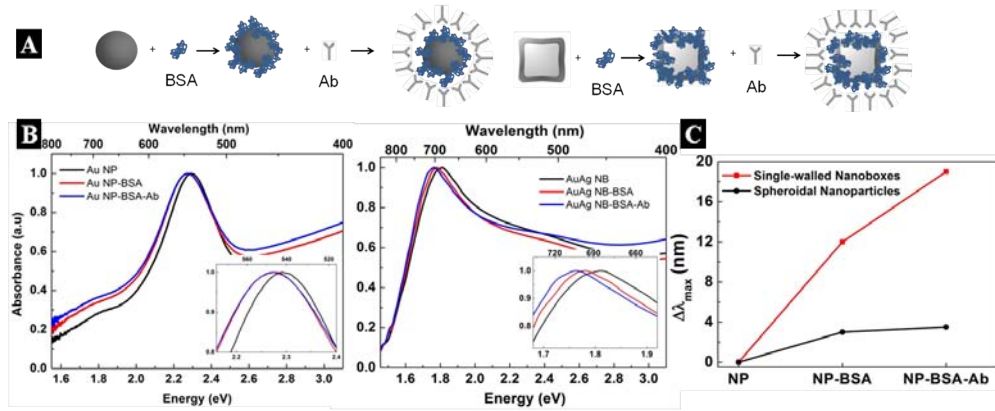


FIGURE 3.50: A. Schematic representation of the primary and secondary protein conjugation processes with spherical Au nanoparticles (left) and single-walled AuAg nanoboxes (right). B. UV-Vis spectra of the unconjugated (black line) spherical Au nanoparticles (left) and single-walled AuAg nanoboxes (right). After the conjugation with BSA (red line) and after the further addition of the Ab (blue line). Insets are details showing the red shift after the binding of the proteins. C. Comparison of the wavelength shift between spherical Au nanoparticles and single-walled AuAg nanoboxes after the first NP-protein interaction and secondary protein-Ab interaction.

around the hollow nanoboxes that allows easy and direct detection of binding events on the vicinity of the nanoboxes.

The sensitivity of the plasmonic nanoparticles can be quantified by using the term sensitivity factor (SF), which is defined as the nanometers of shift in the LSPR peak of the nanoparticle per the refractive index unit (nm/RIU) of the surrounding medium [126]. Thus, a higher SF depicts the generalization of larger shifts in the LSPR peak of the nanoparticle with smaller changes in the refractive index of the surrounding analytes [140].

After experimentally obtaining an enhanced sensitivity with the hollow nanoboxes, we present the comparison of the sensitivities of different Au nanostructures such as 50 nm spherical Au nanoparticles, 50 nm Au nanocubes, 50 nm Au nanoboxes with 7 nm thick walls, 50 nm Au nanoframes with 7 nm walls and a spherical void ($R = 25$ nm) in each face, by using BEM simulations. It should be noted here that we have assumed rounded corners with a radii of 5 nm for the cuboid nanostructures in order to make them more realistic, as discussed above extensively. Sensitivity factors are highly dependent on the shape and composition of the nanostructures [126], for this reason we have used pure Au for all the nanostructures in order to study just the shape effects in sensitivity factors of different nanostructures. Fig. 3.51 shows the BEM simulated UV-Vis spectra of the Au nanostructures in 3 different mediums. Since we have used nanoparticles in water to sense BSA conjugation events experimentally, we assumed a water ambient with a refractive index of $n = 1.33$, which is also used as reference and shown in blue lines. Then, we change the refractive index of the surrounding medium to keep track of the

shifts of LSPR peaks, where UV-Vis spectra shown with green and red lines are obtained by assuming media with refractive indexes of $n = 1.39$ and $n = 1.45$, respectively.

In general, by just looking to the Fig. 3.51, one can see that Au nanoframes have the highest sensitivity to the changes in the environment whereas the spherical Au nanoparticles have the lowest among these nanostructures. More accurately, one can express these changes with the sensitivity factor (SF). BEM simulations revealed that Au spheres have a $SF = 92$ nm/RIU, Au nanocubes have a $SF = 173$ nm/RIU, Au nanoboxes have a $SF = 204$ nm/RIU and Au nanoframes have a $SF = 495$ nm/RIU. Higher sensitivity of the hollow nanostructures is not something unexpected as it is reported in the literature [126, 140, 141] and shown experimentally here. However, it should be underlined here that the SF difference between Au nanocubes and Au nanoboxes, which have essentially the same outer surface area, are a lot lower than the values reported experimentally in the literature. For instance, Sun and Xia [141] compared the sensitivity of Au nanospheres and nanoshells and reported that a SF of 60 nm/RIU measured for the solid nanosphere becomes 409 nm/RIU for the case of a hollow nanoshell of the same size, which corresponds to almost a 7 fold increase in the SF. Similarly, in their review article, Mahmoud et al. [140] tabulated a 5 fold increased SF when comparing Au nanocubes and hollow Au nanocages. Such a discrepancy can have two main reasons, basically due to compositional and morphological differences. Firstly, the presence of Ag in the so-called hollow Au nanostructures may increase the SF of experimentally investigated hollow nanostructures since Ag is known to have better SF than Au [126, 140]. To check the effect of composition, we have simulated the response of 50 nm nanocubes composed of 60 % Au and 40 % Ag (similar to the composition of experimental nanoboxes) and obtained a SF of 181 nm/RIU, which is only 8 nm/RIU higher than the SF of pure Au nanocubes. So, only the compositional differences can not be accounted for the higher SF of the experimental hollow nanoparticles. On the other hand, synthesized hollow nanoshells, nanoboxes or nanocages are known to have multiple voids on the faces [50, 69, 140, 171]. Yet, hollow nanoboxes are simulated as having intact walls. The presence of voids along the nanostructures increases the surface area of the nanostructures and thereby increases the sensitivity.

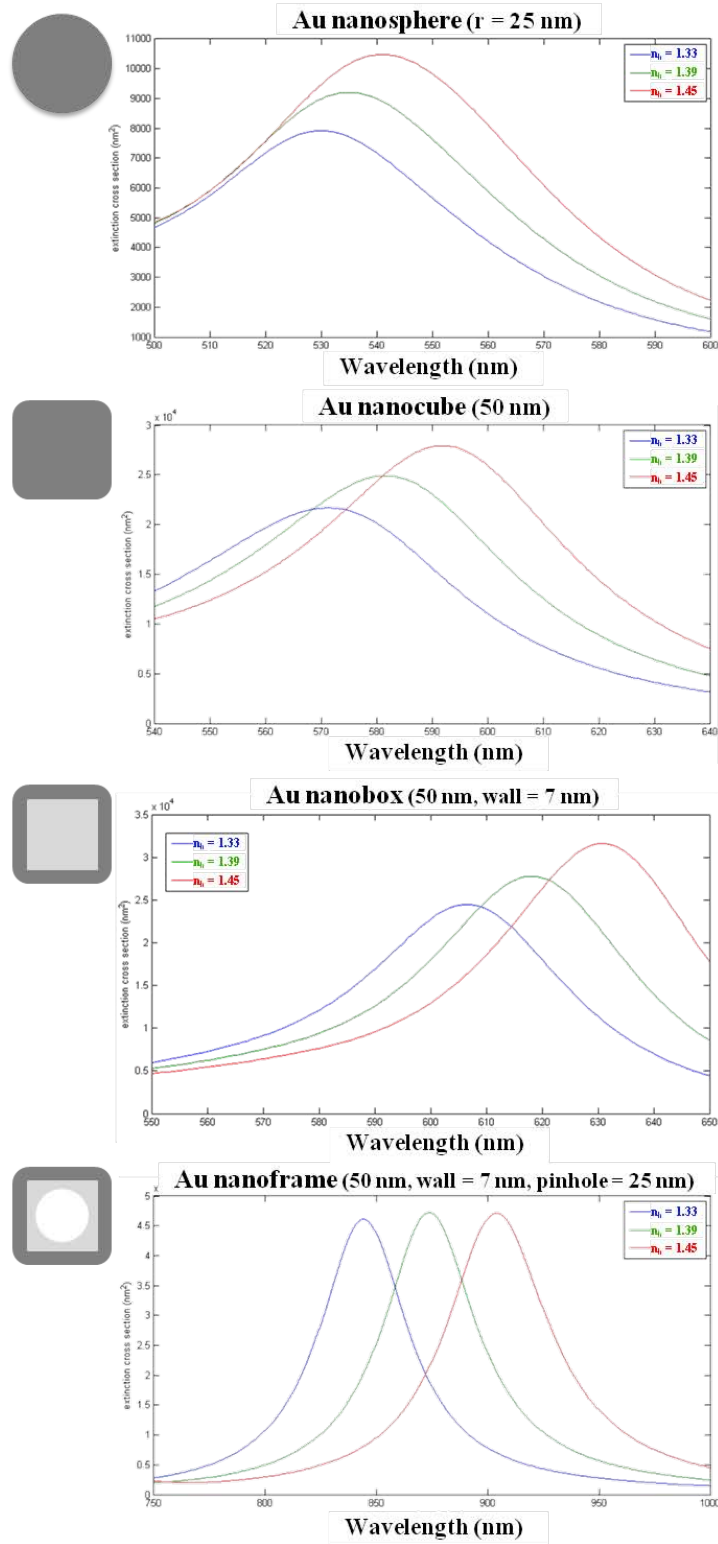


FIGURE 3.51: BEM simulated sensitivity of spherical Au nanoparticles, Au nanocubes, Au nanoboxes and Au nanoframes, against the change in the surrounding medium. Blue spectra are in water with a refractive index $n = 1.33$, green spectra is an environment with a refractive index of $n = 1.39$, red spectra are the case for the medium with a refractive index of $n = 1.45$.

3.9 Summary and conclusions

In this chapter, we have shown the localized surface plasmon resonance properties of several complex metal nanostructures: Ag nanocube, Ag@Au core-shell nanocube, pin-holed AuAg nanobox, single-walled AuAg nanobox, AuAg nanoframe and double-walled AuAg nanobox characterized by low-loss EELS technique in a monochromated STEM microscope with sub-eV energy resolutions at the nanoscale. These nanostructures are synthesized via sequential galvanic replacement and Kirkendall growth processes by using Ag nanocubes as templates [69] and represent different stages of the progressing reaction. We have compared the results obtained by three different data processing techniques of Gaussian fitting, independent component analysis by using blind source separation algorithm and vertex component analysis. We have used BEM simulations in order to be able to better elucidate our experimental results. In this way, we have used Ag nanocubes as a playground to discuss morphological effects and the influence of substrate presence on the plasmonic properties. With the pre-determined morphological and compositional assumptions, we have obtained almost perfect fits between the experimentally collected EEL spectra and BEM simulated EEL spectra of the single-walled AuAg nanoboxes and AuAg nanoframes. As a proof-of-concept experiment for the enhanced plasmonic properties in the hollow nanostructures, we have conducted a sensing experiment where we have compared the response of highly sensitive spherical Au nanoparticles and single-walled AuAg nanoboxes to conjugation events with Bovine Serum Albumin (BSA) and its antibodies (anti-BSA, Ab). In this way, we were able to reveal that hollow nanoboxes show 5 fold increased sensitivity than spherical nanoparticles. We have discussed the sensitivity of different Au nanostructures for the results obtained by BEM simulations, taking the universal merit of sensitivity factor into account.

Figures 3.52A and 3.52B shows the sketches and HAADF STEM micrographs of the investigated nanostructures, respectively. Background subtracted low-loss EEL spectra summed over the nanostructures are shown in Fig. 3.52C, revealing the modulation of the LSPRs induced by the morphological changes. As a general trend, LSPR peaks of the Ag nanocube are shifted to lower energies with the Au alloying and/or increasing of void size for the case of hollow nanostructures. We can anticipate the observed shift to both morphological and compositional effects. However, as discussed throughout the chapter, morphological changes are more dominant than the chemical modifications while determining the plasmonic properties of the nanostructures. Therefore, we conclude that the local compositional differences surely affect the plasmonic properties of AuAg nanostructures such as the cases observed for Ag@Au core-shell nanocubes and

pinholed AuAg nanoboxes, however, the morphological differences induced by these compositional differences in accordance with the galvanic replacement reaction have more dominant effects on the plasmonic properties of the AuAg nanostructures.

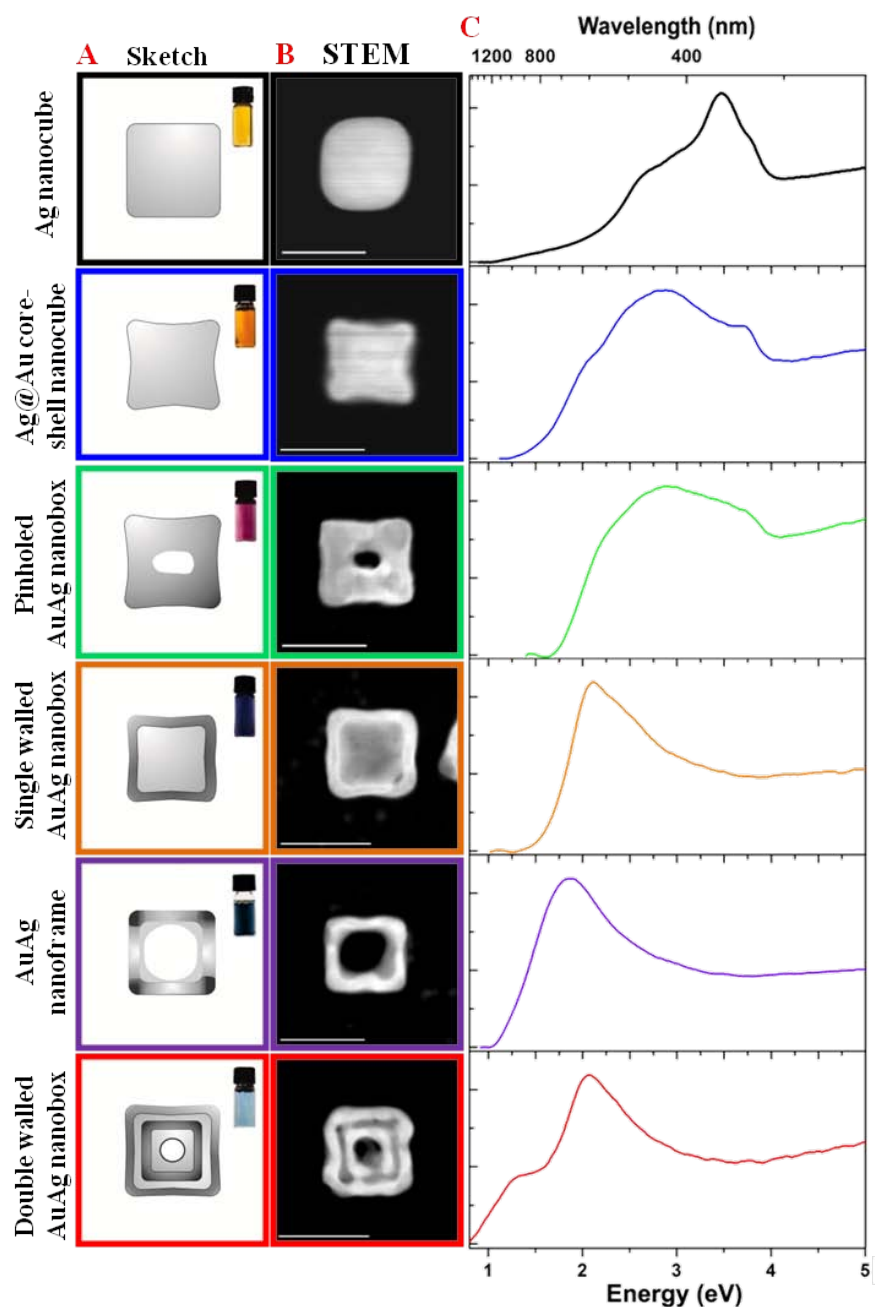


FIGURE 3.52: Structural and LSPR evolution of the AuAg nanostructures. A. Structural sketches and corresponding solution colors of Ag nanocube, Ag@Au core-shell nanocube, pinholed AuAg nanobox, single-walled AuAg nanobox, AuAg nanoframe and double-walled AuAg nanobox. B. HAADF STEM micrographs of the nanostructures where SI EELS have been acquired, from Ag nanocube to double-walled AuAg nanobox (scale bars = 50 nm). C. Summed background subtracted EEL spectra collected over the nanostructures showing the evolution of localized surface plasmon resonances with structural changes.

It has been observed both experimentally and computationally that the number of the plasmon peaks, hence, the number of the components decreases substantially for the hollow nanostructures such as nanoboxes and nanoframes, where one or two main plasmon resonances cover most of the EEL spectra. This is because the plasmon resonances are homogeneously distributed around the hollow nanostructures, which is also revealed experimentally and on the BEM simulated plasmon maps.

It is argued that Ag has better plasmonic properties than those of Au and has higher sensitivity factors. However, it is well-known that Ag is not bio-compatible and can not be used in bio-related sensing applications. Therefore, one needs to use bio-compatible nanostructures such as Au (or at least Au-rich) nanostructures that can have high sensitivities such as Ag. One way of doing so is to make them hollow, as the process and the plasmonic properties of hollow nanostructures have been discussed thoroughly in this study. It has been shown that single-walled AuAg hollow nanoboxes have 5-fold increased sensitivity compared to spherical solid Au nanoparticles against conjugation events with BSA and its antibodies and they are perfect candidates for biosensing applications. Based on the experimentally observed results and/or BEM simulations, one can anticipate that hollow nanoparticles such as AuAg nanoframes or double-walled AuAg nanoboxes would have higher sensitivity than that of single-walled nanoboxes. However, the synthesis procedures for these nanostructures allow us to fabricate the nanoframes and double-walled nanoboxes with low abundances of about 40%, in contrary to the ~90% yield of the single-walled AuAg nanobox synthesis. In this way, we hope to exploit these nanostructures as promising sensors by improving their synthesis routines in the future.